

Variability of the Atlantic off-equatorial eastward currents during 1993–2010 using a synthetic method

Marlos Goes,^{1,2} Gustavo Goni,² Verena Hormann,^{1,2,3} and Renellys C. Perez^{1,2}

Received 17 December 2012; revised 5 March 2013; accepted 26 March 2013.

[1] We have developed, validated, and applied a synthetic method to monitor the off-equatorial eastward currents in the central tropical Atlantic. This method combines high-density expendable bathythermograph (XBT) temperature data along the AX08 transect with altimetric sea level anomalies (SLAs) to estimate dynamic height fields from which the mean properties of the North Equatorial Countercurrent (NECC), the North Equatorial Undercurrent (NEUC) and the South Equatorial Undercurrent (SEUC), and their variability can be estimated on seasonal to interannual timescales. On seasonal to interannual timescales, the synthetic method is well suited for reconstructions of the NECC variability, reproduces the variability of the NEUC with considerable skill, and less efficiently describes variations of the SEUC, which is located in a region of low SLA variability. A positive correlation is found between interannual variations of the NECC transport and two indices based on an interhemispheric sea surface temperature (SST) gradient and southeasterly wind stress in the central tropical Atlantic. The NEUC is correlated on interannual timescales with SSTs and meridional wind stress in the Gulf of Guinea and zonal equatorial wind stress. This study shows that both altimetry and XBT data can be effectively combined for near-real-time inference of the dynamic and thermodynamic properties of the tropical Atlantic current system.

Citation: Goes, M., G. Goni, V. Hormann, and R. C. Perez (2013), Variability of the Atlantic off-equatorial eastward currents during 1993–2010 using a synthetic method *J. Geophys. Res. Oceans*, 118, doi:10.1002/jgrc.20186.

1. Introduction

[2] The upper-ocean zonal current system in the tropical Atlantic is of great importance for both interhemispheric and west-to-east exchange of heat, salt, and nutrients [e.g., Foltz *et al.*, 2003; Brandt *et al.*, 2008; Kirchner *et al.*, 2009]. This system also impacts the climate and weather in the surrounding continental areas [e.g., Sutton and Hodson, 2005; Brandt *et al.*, 2011] since upper-ocean dynamics play an important role in the dominant modes of coupled ocean-atmosphere variability in this region [e.g., Chang *et al.*, 2006, and references therein]. In the western equatorial Atlantic, the northward-flowing North Brazil (Under)Current NB(U)C retroflects eastward, shedding eddies northward along the western boundary [Goni and Johns, 2001], and feeding into the tropical Atlantic zonal current system,

namely the Equatorial Undercurrent (EUC) along the equator, and three off-equatorial currents, the North Equatorial Countercurrent (NECC), the North Equatorial Undercurrent (NEUC), and to a lesser extent the South Equatorial Undercurrent (SEUC) [e.g., Metcalf and Stalcup, 1967; Cochrane *et al.*, 1979; Peterson and Stramma, 1991; Schott *et al.*, 1995, 2003; Boulès *et al.*, 1999; Goes *et al.*, 2005]. These eastward equatorial currents connect the western boundary regime to the interior circulation [e.g., Frantantoni *et al.*, 2000; Hazeleger *et al.*, 2003] and provide water for the eastern upwelling regimes [e.g., Hisard and Hénin, 1987; Hua *et al.*, 2003; Marin *et al.*, 2003; Zhang *et al.*, 2003; Schott *et al.*, 2004; Doi *et al.*, 2007; Stramma *et al.*, 2008].

[3] To date, our knowledge about the eastward current system in the equatorial Atlantic arises from numerical models as well as in situ and satellite observations, which have either limited spatial or temporal coverage. Although the seasonal to interannual variations of the NECC and EUC have been studied extensively [e.g., Richardson and Reverdin, 1987; Garzoli and Richardson, 1989; Goes and Wainer, 2003; Fonseca *et al.*, 2004; Arhan *et al.*, 2006; Hormann and Brandt, 2007; Brandt *et al.*, 2008; Kolodziejczyk *et al.*, 2009; Hormann *et al.*, 2012], the low-frequency variability of the off-equatorial undercurrents, the SEUC and the NEUC, is less well known [Schott *et al.*, 2003; Fischer *et al.*, 2008; Hüttl-Kabus and Böning, 2008]. Upper-ocean currents in the equatorial Atlantic are modified by wind forcing [e.g., Philander and Pacanowski, 1986;

¹Cooperative Institute for Marine and Atmospheric Studies, University of Miami, Miami, Florida, USA.

²Atlantic Oceanographic and Meteorological Laboratory, National Oceanic and Atmospheric Administration, Miami, Florida, USA.

³Now at Scripps Institution of Oceanography, University of California–San Diego, La Jolla, California, USA.

Corresponding author: M. Goes, Cooperative Institute for Marine and Atmospheric Studies, University of Miami, Miami, FL 33149, USA. (marlos.goes@noaa.gov)

Katz, 1987; Yang and Joyce, 2006] and oceanic mesoscale phenomena, such as tropical instability waves (TIWs) [e.g., Düing et al., 1975; Weisberg and Weingartner, 1988; Menkes et al., 2002; Grodsky et al., 2005; Athié et al., 2009] that can alias estimates of the seasonal to interannual variability obtained from observational systems that are not continuous in time. Indeed, the NEUC and SEUC are relatively weak and diffusive currents, and as such, they are more susceptible to aliasing from TIWs when not enough observations have been carried out [Schott et al., 2003; Jochum and Malanotte-Rizzoli, 2004; Fischer et al., 2008]. Because of the enhanced TIW activity in the northern hemisphere [e.g., Foltz et al., 2004; Athié and Marin, 2008], the seasonal overlap between the NEUC and the EUC in the western part of the basin [e.g., Boulès et al., 1999; Schott et al., 2003; Goes et al., 2005], and the NEUC and NECC in the central part of the basin [e.g., Stramma and England, 1999; Stramma et al., 2005; Brandt et al., 2010], more analysis and study of the NEUC, in particular, is needed.

[4] An existing observational system that can potentially resolve the short spatial and temporal scales and allow for quantification of the seasonal to interannual variability of the eastward currents is satellite altimetry. Since upper-ocean currents with weak sea level height (SLH) signatures cannot be resolved from surface topography fields alone [Goni and Baringer, 2002], an empirical relationship between certain current features and their SLH characteristics can sometimes be constructed using a synthetic method to overcome this sampling challenge. This can be achieved by combining altimetry data with those from other observational platforms, such as high-resolution hydrographic data. Several past studies have combined altimetric and hydrographic observations obtained from expendable bathythermographs (XBTs), conductivity-temperature-depth (CTD) measurements, or Argo float profiles to infer properties of the upper ocean, such as velocity, temperature, and salinity as well as volume, heat, and salt transports, mostly in the Pacific and Atlantic oceans at higher latitudes [e.g., Goni et al., 1996; Gilson et al., 1998; Phillips and Rintoul, 2002; Rintoul et al., 2002; Ridgway et al., 2008; Gourcuff et al., 2011]. Although a few studies have attempted to apply synthetic methods to the tropical Atlantic [Carton and Katz, 1990; Arnault et al., 1999, 2011], a thorough analysis of their utility for monitoring upper-ocean currents in the tropical Atlantic has yet to be performed.

[5] The goals of this study are to quantify the variability of the surface and subsurface Atlantic off-equatorial eastward currents in terms of their volume transport, velocity, and location on seasonal timescales, and to explore how interannual changes in their transport relate to the tropical Atlantic climate modes. To accomplish these goals, we consider a monitoring system that relies upon data from the cross-equatorial high-density XBT transect AX08 during 2000–2010, and from satellite altimetry observations to generate synthetic time series from which the variability of the eastward currents in the equatorial Atlantic can be analyzed during the 1993–2010 altimetric period. The high-density XBT project has been active for over 20 years, and aims at sustainably measuring physical properties of the upper ocean with mesoscale resolution. Its high spatial resolution and repeated sampling of the region enable assessment of upper-ocean temperature, heat storage and

transport variability, and permit analysis of the variability of major geostrophic currents. The data sets used in this study are described in section 2. In sections 3 and 4, the methodology applied to blend altimetry and XBT data is explained and validated for the NECC, NEUC, and SEUC, respectively. The ability of these observations to capture their seasonal variability is examined in section 4. The interannual variability of the off-equatorial eastward currents that are well resolved by this synthetic method, namely the NECC and NEUC, is also examined in section 4, and linked to tropical Atlantic coupled climate modes. Discussion, conclusions, and recommendations for future improvements of the methodology are provided in section 5.

2. Data

[6] A description of each of the data sets used in this study to quantify the variability of the Atlantic off-equatorial eastward currents is given below.

2.1. Hydrographic Data

[7] The temperature data used in this study correspond to 39 realizations of the AX08 XBT transect, which is carried out between Cape Town and New York City and crosses the equator at about 23°W (Figure 1a). The first section was obtained in December 2000, and an average of four realizations per year has been achieved since 2002. Approximately 200–300 XBTs are deployed during each AX08 transect, with an average spacing of 25 km between casts in the tropics, between 20°S–20°N. Sippican Deep Blue XBT probes are used, which have a nominal depth range of 760 m, but typically reach depths of 850 m for standard ship velocities [Hanawa et al., 1994]. XBT measurements are performed by sampling temperature and the elapsed time of descent of the XBT probes. The time of descent (t in seconds) is converted to depth (z in meters) using the standard manufacturer's fall rate equation (FRE), that is $z = 6.472t - 0.00216t^2$.

[8] In order to study the variability of the off-equatorial eastward currents, we restrict the observations to a region with similar dynamical characteristics. We define a criterion that selects the sections whose mean longitude between 10°S and 10°N lies within one standard deviation of the median value of all sections (Figure 1b). To calculate the median and standard deviation of the position of all sections, we apply a bootstrap method [Johnson, 2001]. The median longitude of the AX08 transect, which is about 40° oblique with respect to a true meridional section, is approximately 23°W (Figure 1a). Additionally, we exclude the September 2004 section from the analysis because its derived surface dynamic height shows a spatial mean bias relative to the other AX08 sections. The applied constraints reduce the number of transects from 39 to 31 (Figure 1c), but assure that we are working with comparable data.

[9] For these 31 sections, individual temperature profiles are linearly interpolated onto a 2 m vertical grid. The data are quality controlled by excluding outlier profiles, or profiles whose both forward and backward horizontal gradients of the surface dynamic height lie outside the three-standard-deviation range of all profiles. Next, the sections are horizontally interpolated to a uniform 0.2° latitude grid,

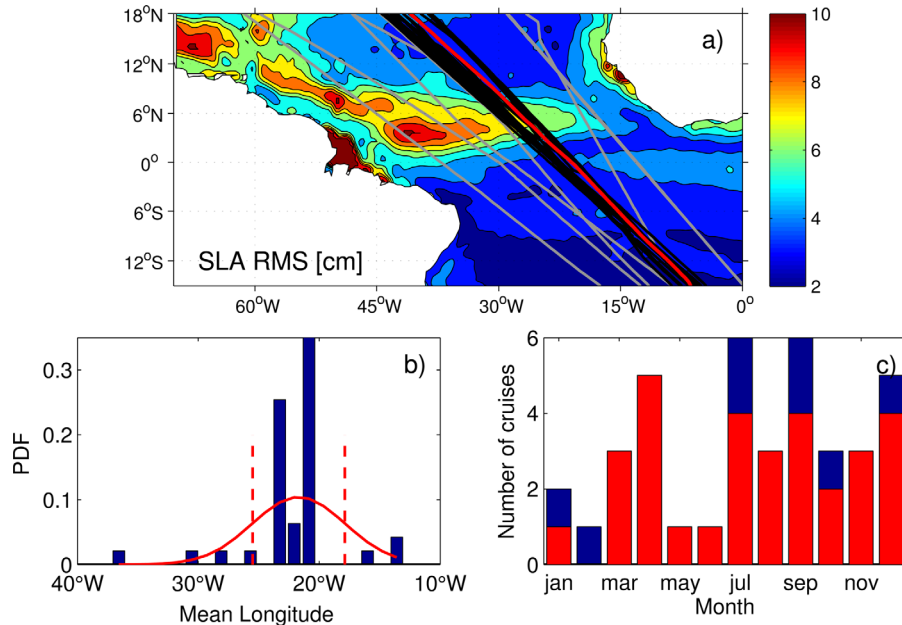


Figure 1. (a) Root-mean-square error of October 1992–December 2010 AVISO SLA (cm) in the tropical Atlantic (filled contours), with superimposed AX08 sections: the 31 selected sections (black lines), the eight sections not included in the analysis (gray lines), and mean of the selected sections (red line). (b) Probability density function of the averaged longitude between 10°S and 10°N for all the AX08 XBT sections. Red line is the bootstrapped distribution, with one standard deviation ($1-\sigma$) marked by dashed lines. (c) Histogram of the number of sections per month before (blue bars) and after (red bars) the selection of the sections that fall inside the $1-\sigma$ of b).

which matches the nominal resolution of the AX08 transect in the tropics. To achieve this, we use an optimal interpolation scheme based on a Gaussian correlation function with a decorrelation length scale of 1.25° and a low noise-to-signal ratio of 0.05, similar to *Brandt et al.* [2010], which is a trade-off between smoothing data noise and preserving the spatial scales of the equatorial currents. Salinity is derived from the XBT temperature profiles [*Thacker, 2007a, 2007b*] using climatological temperature-salinity (T - S) relationships extracted from the 2009 *World Ocean Atlas* (WOA09) [*Locarnini et al., 2010*], and gridded at latitude, longitude, and depth locations. Specific errors are associated with XBT measurements due to temperature precision and depth estimation in the tropical Atlantic [e.g., *Reverdin et al., 2009*], and salinity inference from climatological T - S relationships [e.g., *Goni and Baringer, 2002*]. A discussion of the uncertainties associated with XBT measurements, including the oblique orientation of the AX08 transect, is provided in the Appendix.

2.2. Altimetric Data

[10] Here we use the Archiving, Validation, and Interpretation of Satellite Oceanographic data (AVISO) reference (“ref”) delayed mode product (<http://www.aviso.oceanobs.com>), which blends data from two satellites out of a variable constellation of satellites [*Le Traon et al., 1998*], and provides homogeneous, gridded, optimally interpolated, and cross-calibrated global coverage of sea level anomalies (SLAs) relative to the 1993–1999 mean. The SLA-delayed mode data are continuously available on a $1/3^\circ$ horizontal grid with daily temporal resolution since October 1992 and precision of 2 cm [*Cheney et al., 1994; Ducet et al., 2000*].

In this study, we use data from October 1992 to December 2010, subtract the 2000–2010 mean SLA field for consistency with the zero-mean anomalies of dynamic height in the XBT data set for this period, similar to *Ridgway et al.* [2008], and detrend by subtracting the 2 year moving average time series of the tropical Atlantic SLA basin average to be able to obtain static linear relationships with the XBT dynamic height. We further interpolate the SLAs linearly onto the location and time of the individual XBT sections to estimate regression parameters for the synthetic method (section 3), and onto the mean AX08 transect to produce a hindcast of the currents for the 1993–2010 altimetric period.

2.3. Reference Dynamic Height

[11] We use referenced dynamic heights from the monthly climatology of the International Pacific Research Center (IPRC) (<http://apdrc.soest.hawaii.edu>). This data set is available on a $1^\circ \times 1^\circ$ horizontal grid at 27 depth levels and is derived from Argo floats and altimetry observations, with the mean sea level referred to the mean dynamic topography MDT_CNES-CLS09 [*Rio et al., 2011*]. We use the IPRC dynamic height (DH_{IPRC}) at 800 m depth, interpolated horizontally onto the regularized XBT grid.

2.4. Sea Surface Temperature and Pseudowind Stress

[12] To explore how interannual changes in the transport of the off-equatorial eastward currents relate to the tropical Atlantic climate modes, we use gridded sea surface temperature (SST) and pseudowind stress data. SSTs are extracted from the NOAA optimum interpolation (OISST-v2) analysis [*Reynolds et al., 2007*], which is available daily on a $1/4^\circ$ horizontal grid since November 1981.

[13] The pseudowind stress data are obtained from the cross-calibrated, multiplatform (CCMP), multi-instrument ocean surface wind velocity data set. This product combines data derived from multiple satellites using a variational analysis method to produce a consistent record of ocean surface vector winds at 25 km horizontal resolution and is available since July 1987 every 5 days [Atlas *et al.*, 2011]. For our purposes, both data sets are interpolated to 7 day increments and mapped onto a $1/4^\circ \times 1/4^\circ$ Mercator grid.

3. Methodology

3.1. Velocity Calculation

[14] We calculate the cross-sectional absolute geostrophic currents from horizontal gradients of absolute dynamic height (DH) using the thermal wind relationship. The XBT-derived dynamic height (DH_{XBT}) is computed using XBT temperature and depth information, and salinity inferred from climatological T - S relationships (section 2.1). To obtain DH for each XBT profile, we reference DH_{XBT} to the IPRC monthly climatology of absolute dynamic height (DH_{IPRC}) at 800 m:

$$DH(z) = DH_{\text{XBT}}(z) + DH_{\text{IPRC}}(800 \text{ m}). \quad (1)$$

[15] Although the inclusion of DH_{IPRC} does alter the mean DH significantly, the DH horizontal gradients are not greatly affected ($O(10^{-7})$ cm/km change) by this referencing. Geostrophy has an inflection point at the equator, thus requiring the use of the equatorial beta-plane approximation for velocity calculation near the equator, which relies on the computation of higher-order DH derivatives. Here, we apply the method of Lagerloef *et al.* [1999], which uses a third-order polynomial fit for the estimation of geostrophic velocities within $\pm 3^\circ$ of the equator. Due to the large uncertainty resulting from this method, we do not focus on the EUC in the present study.

3.2. Synthetic Method

[16] Altimetry and XBT data are here combined to provide a broader four-dimensional (i.e., spatial and temporal) coverage of the equatorial eastward currents in the tropical Atlantic. Several studies have combined altimetric and hydrographic observations to infer properties of the upper ocean [e.g., Carnes *et al.*, 1994; Goni *et al.*, 1996; Gilson *et al.*, 1998; Arnault and Kestenare, 2004; Phillips and Rintoul, 2002; Ridgway and Dunn, 2010], using the vertical coherence of the ocean as a basis for deriving such relationships. The skill of these synthetic methodologies varies among different regions of the ocean [Guinehut *et al.*, 2006], since altimetry captures both steric and nonsteric components, and in some regions the nonsteric contributions, such as the barotropic component, can account for more than 50% of the total sea level variability [Shriver and Hurlburt, 2000]. More recently developed synthetic methodologies use, for example, bottom pressure information to subtract the nonsteric component of the SLH, which is widely used in assimilation models [e.g., Shriver and Hurlburt, 2000; Barron *et al.*, 2007], empirical orthogonal functions to build depth-dependent relationships throughout the water column [Fox *et al.*, 2002], and a combination of

altimetry, in situ and gravimetric data (e.g., GRACE) to study the sea level variability [Willis *et al.*, 2008; Leuliette and Miller, 2009].

[17] In this study, we apply a synthetic method to produce a hindcast of along-track DH and potential density (σ_θ), as well as across-track velocity for the mean AX08 transect position (red line in Figure 1a). Since we are interested in velocity distributions along isopycnal layers, we seek as predictands σ_θ and DH from the surface down to 800 m, and use altimetric SLA data as predictors. Our methodology is based on a simple linear regression, which is the most parsimonious choice for this type of analysis, and consists of two steps:

[18] Step 1: Data from the 31 selected XBT sections are used to build linear relationships between the surface dynamic height (DH_0) and the two predictands, which are defined at each depth (z) and latitude (y):

$$\begin{aligned} DH^{\text{anom}}(z, y) &= DH_0^{\text{anom}}(y)\alpha_1(z, y) + \beta_1(z, y), \\ \sigma_\theta^{\text{anom}}(z, y) &= DH_0^{\text{anom}}(y)\alpha_2(z, y) + \beta_2(z, y), \end{aligned} \quad (2)$$

where anomalies (superscript “anom”) are calculated with respect to the monthly climatological field, and the parameters α_i and β_i ($i = 1, 2$) correspond to the slopes and intercepts of the regression, respectively. The σ_θ and DH climatological fields are derived from the WOA09 monthly climatology. Consistent with the absolute DH estimated from the XBT data, we also apply the IPRC climatology (DH_{IPRC}) as the reference for DH^{clim} at 800 m. The skill of this method to monitor the variability of the predictands DH^{anom} and $\sigma_\theta^{\text{anom}}$ is demonstrated by the temporal correlation between DH_0^{anom} and the predictands at each depth and latitude (Figure 2). As expected, correlations are predominantly positive for DH^{anom} and negative for $\sigma_\theta^{\text{anom}}$ since dynamic height is calculated from specific volume anomalies, which are inversely related to density [Pond and Pickard, 1983]. Apart from their sign, both fields show similar relationships, with highest correlations in the upper 200 m of the water column, and decreasing correlation values with depth. At certain latitudes, such as in the vicinity of 5°N , high correlations ($R \approx 0.8$) can extend from the surface down to 800 m depth.

[19] Step 2: Finally, DH_0 is linearly regressed onto SLA, forming the link between the altimetric and hydrographic observations:

$$DH'_0 = DH_0 - \overline{DH_0} = \text{SLA} \varphi_1 + \varphi_2, \quad (3)$$

where DH'_0 is the deviation from the mean of all sections, denoted by $\overline{DH_0}$, such that DH'_0 and SLA have approximately zero mean during the AX08 period, and φ_1 and φ_2 correspond to the respective slope and intercept of the regression. DH'_0 and SLA are well correlated ($R = 0.89$), with a root-mean-square error (RMSE) = 2.07 cm and a negligible intercept or bias (Figure 3d). This strong relationship between the two variables indicates that the SLA captures well the baroclinic structures in the region, especially the first mode [Gilson *et al.*, 1998; McCarthy *et al.*, 2000; Guinehut *et al.*, 2006]. The highest SLA variance occurs between 3° and 8°N (Figure 3a), coincident with the largest horizontal SLA gradients that are closely related to

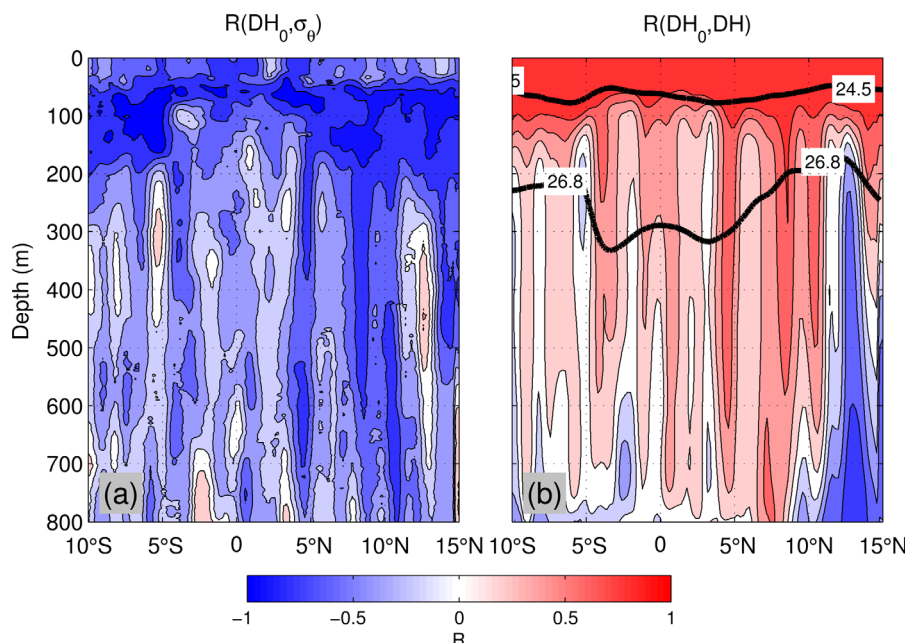


Figure 2. Correlation at each depth and latitude between surface dynamic height anomalies (DH_0^{anom}): (a) density anomalies ($\sigma_\theta^{\text{anom}}$) and (b) dynamic height anomalies (DH_0^{anom}). The thick black lines in Figure 2b mark the mean depth of the isopycnals $\sigma_\theta = 24.5 \text{ kg m}^{-3}$ and $\sigma_\theta = 26.8 \text{ kg m}^{-3}$ that define the upper and lower current layers, respectively.

the strength of the NECC [e.g., *Arnault et al.*, 2011]. Less variability is observed south of the equator, which may be due to compensating effects in the water column [*Mayer et al.*, 2001].

4. Results

[20] The temperature, salinity, and zonal geostrophic velocity estimated along the AX08 sections are represented during all seasons in the central tropical Atlantic (Figure 4). The seasonal-mean temperature distributions in this region (Figures 4a–4d) are characterized by a warm (generally above 25°C) and well-mixed surface layer, where the tropical surface water (TSW) is located in the upper 50–80 m, or above $\sigma_\theta = 24.5 \text{ kg m}^{-3}$. Underneath the surface layer, there is a sharp vertical temperature gradient of approximately 0.1°C/m near 100 m depth that marks the upper thermocline. Strong seasonal variations are observed in the upper 200 m of the water column, driven by the asymmetric hemispheric insolation. The corresponding salinity distributions (Figures 4e–4h) are characterized by high salinity values ($>36.5 \text{ psu}$) to the north and south of the displayed domain above the thermocline, characteristic of the subtropical underwater (SUW). These high salinity waters are formed in the subtropics and advected equatorward by the North and South Equatorial Currents. Underneath the SUW is the central water (CW), characterized by a nearly straight line in the T - S space [e.g., *Stramma and England*, 1999]. The upper central water (UCW) is located above $\sigma_\theta = 26.8 \text{ kg m}^{-3}$ [*Kirchner et al.*, 2009] and forms the thermostat between 12°C and 15°C found in the equatorial region [e.g., *Reverdin et al.*, 1991], at the depths of the NEUC and SEUC [e.g., *Cochrane et al.*, 1979; *Schott et al.*, 1995, 1998].

4.1. Identification of the Eastward Current Bands

[21] The seasonal structure of the geostrophic zonal currents in the AX08 data is shown in Figures 4i–4l. North of the equatorial band, the seasonal mean NECC appears at the surface distributed in several narrow eastward flowing cores, which suggests that their seasonal means may be aliased by mesoscale phenomena (e.g., by eddies and TIWs), given the limited number of available samples for each season. Despite this, a broader and well-defined NECC core is observed in boreal winter, summer, and fall (Figures 4i, 4k, and 4l), when DH_0 gradients are larger north of 5°N . A double NECC core structure develops during boreal fall between 5°N and 10°N (Figure 4l), consistent with previous studies [e.g., *Didden and Schott*, 1992; *Urbano et al.*, 2006]. During late boreal spring, DH_0 is nearly flat between 10°S and 10°N (Figure 4b, top), yielding smaller seasonal mean surface geostrophic velocities (Figure 4j).

[22] The results obtained here indicate that during some seasons there is a latitudinal overlap between the surface NECC and the eastward flow in the thermocline layer, when the NEUC can be found as a lobe attached to the NECC (cf. Figure 4i). During boreal spring, the NEUC is clearly detached from the NECC (Figure 4j), but the influence of the NECC is observed as another subsurface branch north of 5°N consistent with *Brandt et al.* [2010]. The signature of the NEUC on the $\sigma_\theta = 26.8 \text{ kg m}^{-3}$ isopycnal is observed at approximately 5°N and 200 m, as a sharp meridional gradient during boreal winter/spring (Figures 4i and 4j) and relatively weaker gradients during the rest of the year [cf. *Bourlès et al.*, 2002; *Schott et al.*, 2003]. The NEUC seasonal means are weakest in boreal summer/fall (Figures 4k and 4l), as observed when comparing velocities

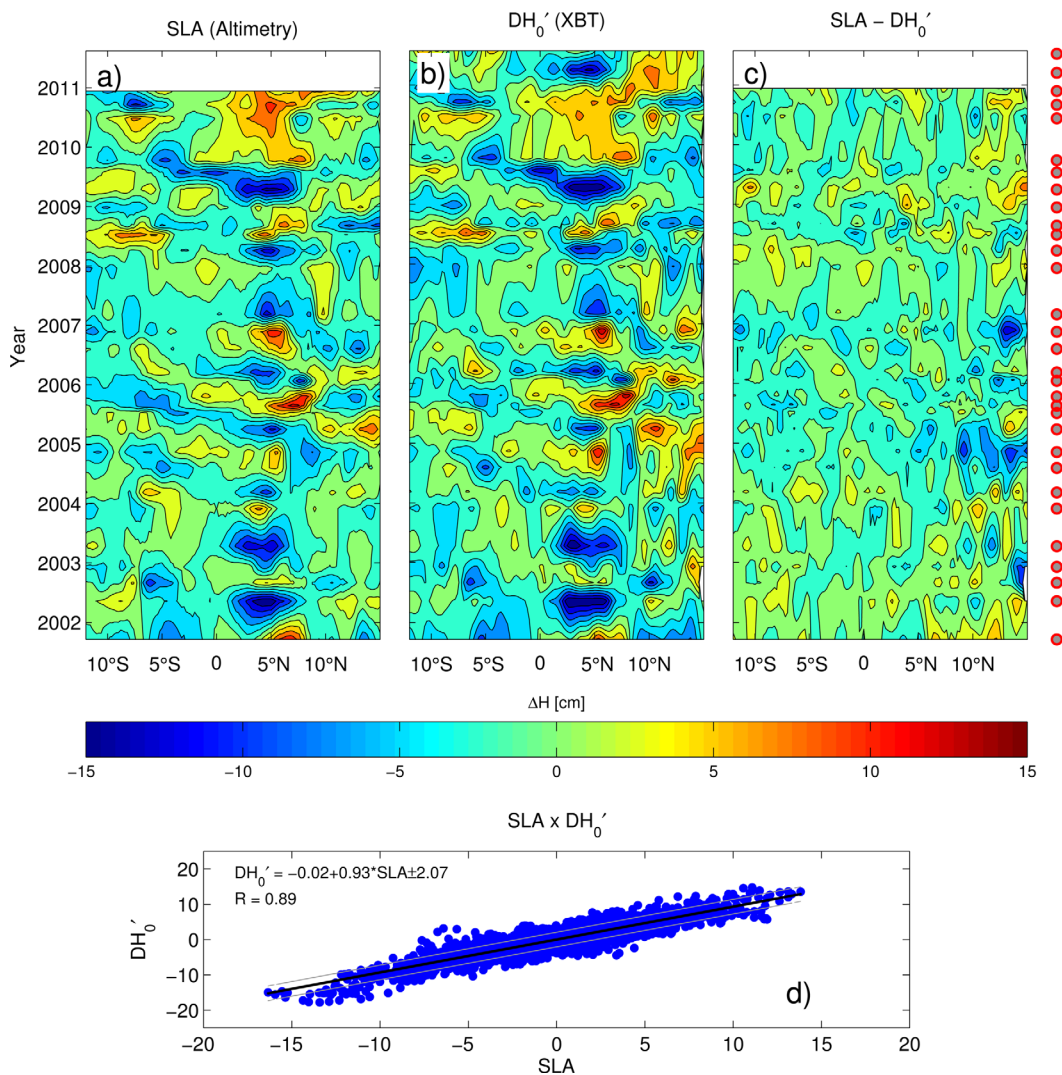


Figure 3. Comparison between SLA and surface dynamic height anomalies (DH'_0): Longitude-time diagrams of (a) SLA, (b) DH'_0 , and (c) $SLA - DH'_0$; dots on the right-hand side of Figure 3c mark the realizations of the AX08 XBT transect. (d) Linear fit between DH'_0 and SLA (thick black line) and its RMSE (gray lines).

in boreal winter/spring with boreal summer/fall. In contrast, the potential density structure at about 4°–5°S and 200 m, where the SEUC is located, exhibits a very distinguished southward elevation of the $\sigma_\theta = 26.8 \text{ kg m}^{-3}$ isopycnal surface that is visible throughout the year. This is an indication that the meridional pressure gradient plays an important role in SEUC dynamics and that the SEUC is a permanent feature of the tropical Atlantic.

[23] To compute quantities associated with the off-equatorial eastward currents, the meridional and vertical extent of each current must be defined. We assign latitudinal bands to each current based on the variability of their observed positions (cf. Figure 4i–4l) that are similar to the bands used in previous studies: The NECC is defined between 3°N and 10°N [e.g., Garzoli and Katz, 1983; Hormann et al., 2012], the NEUC between 3°N and 6°N [e.g., Hüttl-Kabus and Böning, 2008], and the SEUC between 3°S and 6°S [Molinari, 1982, 1983; Hüttl-Kabus and Böning, 2008] (Table 1). Note that, as previously mentioned, the NEUC core location

is highly variable, but in order to avoid the equatorial band (<3° of the equator) and to differentiate the NEUC from subsurface flow observed under the northern branch of the NECC (cf. Figure 4j; Brandt et al. [2010]), we use for this current the same band as defined by Hüttl-Kabus and Böning [2008]. We further characterize these currents by selecting isopycnal layers to define their vertical boundaries following their water masses characteristics [Schott et al., 1998]: an upper or surface layer containing TSW from the surface to $\sigma_\theta = 24.5 \text{ kg m}^{-3}$, and a lower or thermocline layer containing SUW and UCW between $\sigma_\theta = 24.5$ and 26.8 kg m^{-3} . Therefore, in this study, the NECC is restricted to the upper layer, and the NEUC and SEUC are both restricted to the lower layer. Although our choice of vertical and latitudinal boundaries are the most widely used, we recognize that other definitions have also been used in previous studies, including using the thermocline as a vertical boundary for the NECC [Garzoli and Katz, 1983] as well as a time-varying latitudinal characterization of the NECC band centered on the core

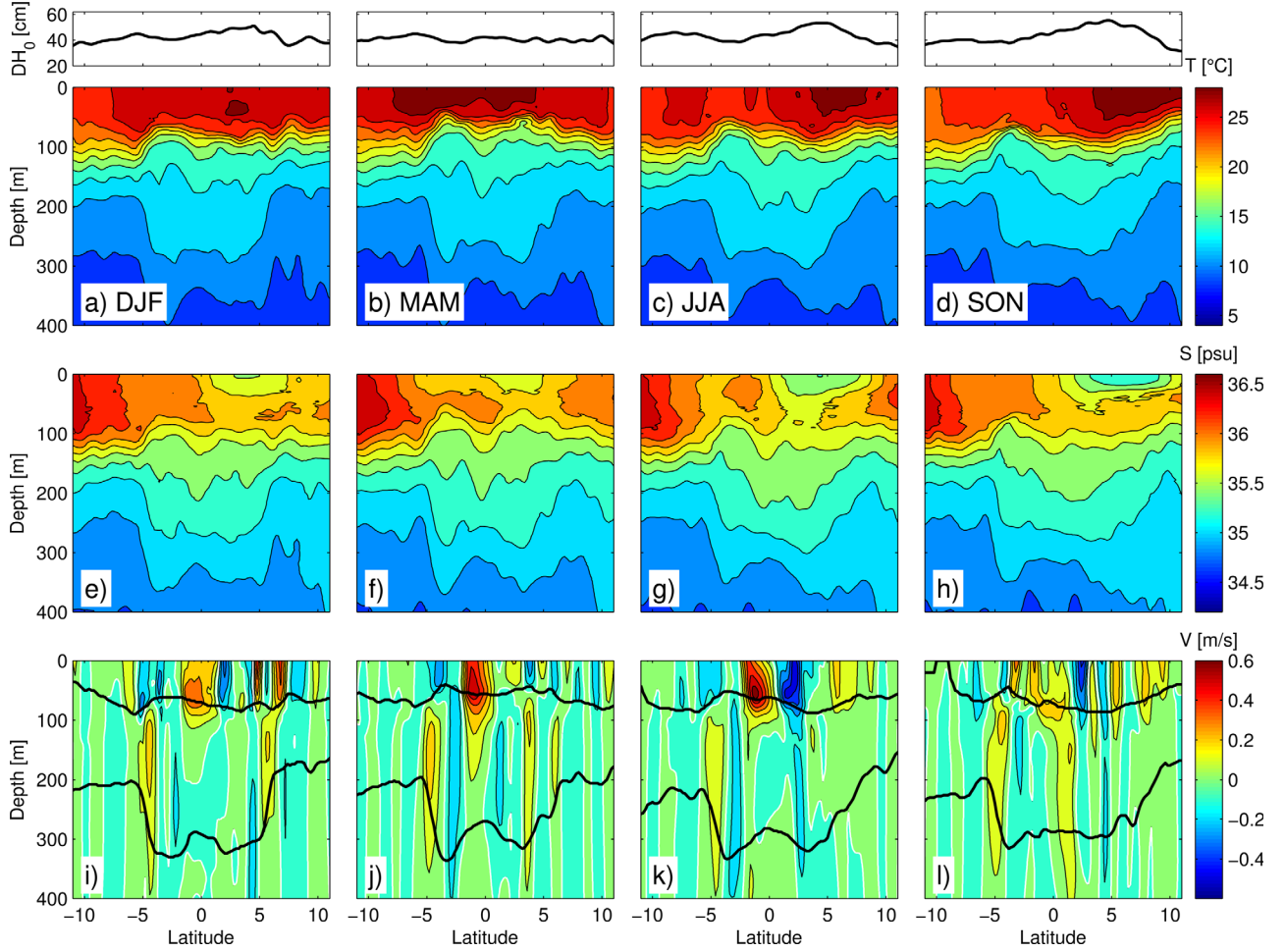


Figure 4. Mean seasonal sections of (a–d) temperature, (e–h) salinity, and (i–l) cross-section velocity derived by fitting the annual and semiannual harmonics to the XBT data. The four columns are each for one seasonal average, displayed in the temperature sections. The black lines overlaid onto the velocity sections are the $\sigma_{\theta} = 24.5 \text{ kg m}^{-3}$ and $\sigma_{\theta} = 26.8 \text{ kg m}^{-3}$ isopycnals used to define the eastward current layers. The seasonal-mean absolute surface dynamic height is shown on the top portion of each column.

latitude or center of mass [Hsin and Qiu, 2012], and for the NEUC and SEUC a depth range from 100 to 700 m [Molinari, 1982] or $\sigma_{\theta} = 25.5$ to 26.8 kg m^{-3} [Hüttel-Kabus and Böning, 2008].

4.2. Seasonal Variability of the Off-Equatorial Eastward Currents in the AX08 Data

[24] Here we analyze the seasonal variability of the NECC, NEUC, and SEUC across the AX08 transect in terms of volume transport, core velocity, and core latitude using monthly averaged values (Figure 5 and Table 2), and compare with previously published values. The selected 31

Table 1. Latitudinal and Isopycnal Ranges Used in the Volume Transport Calculations of the Atlantic Off-Equatorial Eastward Currents

Current	Latitude	σ_{θ} (kg m^{-3})
NECC	3°N–10°N	0–24.5
NEUC	3°N–6°N	24.5–26.8
SEUC	6°S–3°S	24.5–26.8

AX08 temperature sections provide high spatial resolution coverage of the central tropical Atlantic for all months except February (Figure 1c). To investigate the seasonal variability of the studied currents, we fit in a least-squares fashion the annual and semiannual harmonics to the XBT-derived monthly averages (red dots in Figure 5) of the volume transport, core velocity, and core latitude for each current. We use as observational uncertainties in the XBT data the sum of the fitting residual error from the harmonic analysis plus the standard error of each month (when available) after calculating the monthly averages. Fitting the first two annual harmonics interpolates the seasonal cycle to the missing month and gives an error estimate as well as filters a large fraction of the mesoscale signal.

[25] For each current, the seasonal cycle of the XBT-derived monthly averages of volume transport, core velocity, and core latitude (red lines in Figure 5) can be characterized as follows:

4.2.1. North Equatorial Countercurrent

[26] The XBT-derived seasonal cycles show a strong annual cycle of the NECC, which alone represents 72% of the transport variability. Earlier analyses based on drifter data

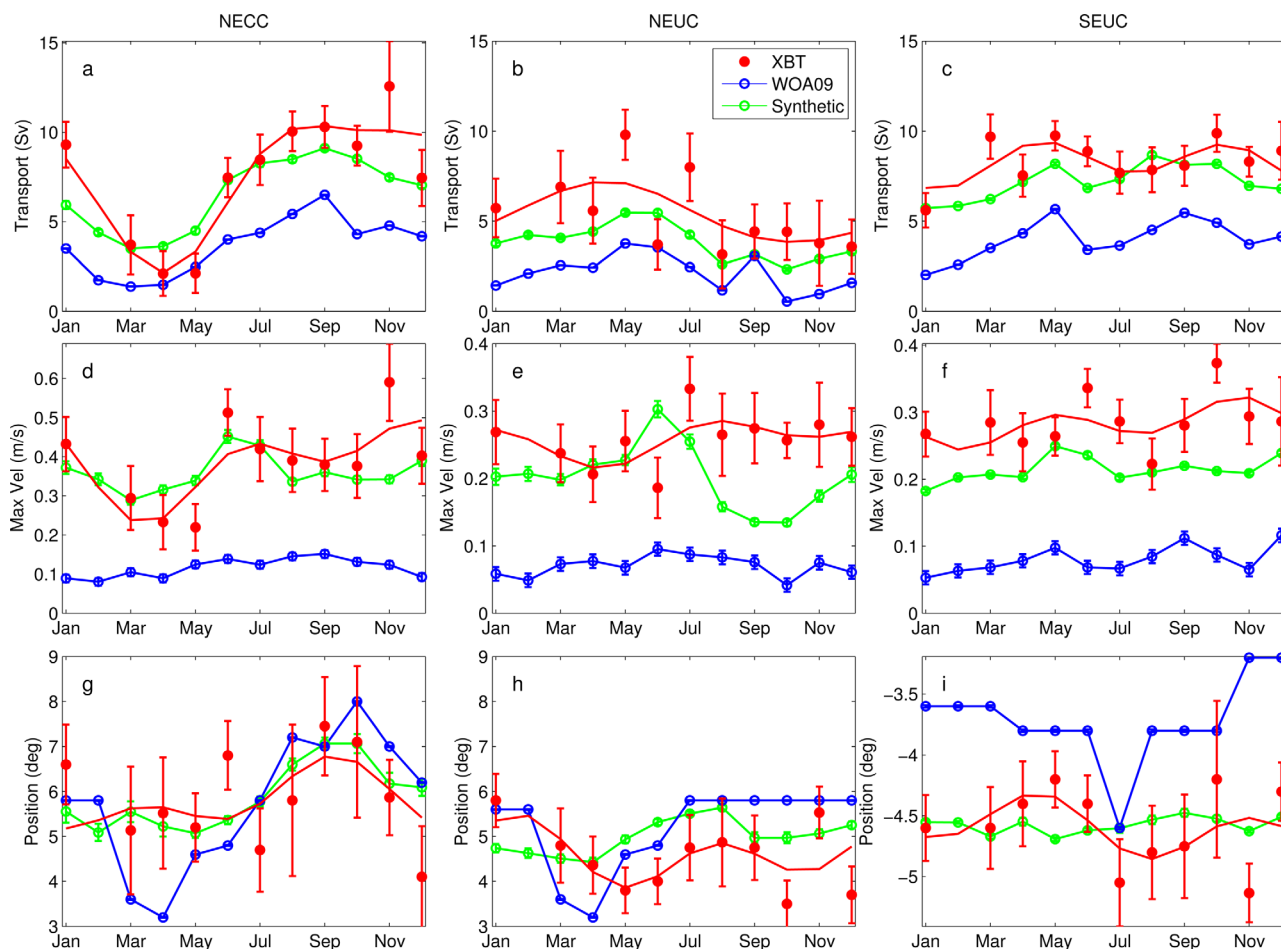


Figure 5. Seasonal cycle of geostrophic volume transport (Sv), core velocity (m/s), and latitudinal position (degrees) for the (a, d, g) NECC, (b, e, h) NEUC, and (c, f, i) SEUC. Red dots are monthly XBT averages and red lines represent the corresponding fit of annual and semiannual harmonics; blue lines represent the WOA09 monthly climatology estimates, and green lines mark the monthly mean synthetic estimates during 1993–2010. Shown error bars are the standard errors for the synthetic estimates, and the standard error plus fitting error for the XBT data.

have already indicated a dominant annual contribution, as high as 80%, to the transport seasonal cycle of the off-equatorial surface currents [e.g., *Richardson and Walsh, 1986; Lumpkin and Garzoli, 2005*]. The NECC reaches its lowest transport (~ 2 Sv) during boreal spring and higher transports (~ 10 Sv) during boreal summer and fall, which agrees with transport values in *Fonseca et al. [2004]*. The

Table 2. Percentage of the Variance of Geostrophic Volume Transport, Core Velocity, and Position Explained by the Annual and Semiannual Harmonics for Each Current Band Using the XBT Estimates

Current	Transport (%)		Core Velocity (%)		Position (%)	
	Annual	Semiannual	Annual	Semiannual	Annual	Semiannual
NECC	72	7	33	23	16	9
NEUC	35	1	21	12	13	31
SEUC	7	39	11	23	9	15

annual cycle is also the dominant component of the core velocity (33%) and position variances (16%; Table 2). The NECC core velocity shows a similar pattern (Figure 5d), with lowest values (~ 0.2 m/s) during boreal spring and higher values throughout the rest of the year (~ 0.4 – 0.5 m/s). The NECC core reaches its southernmost position in boreal spring and early summer ($\sim 5^\circ$ N) and its northernmost position ($\sim 7^\circ$ N) during boreal fall (Figure 5g). This seasonal variability of the NECC agrees with previous observational findings [e.g., *Richardson et al., 1992*] and is linked to the north-south migration of the Intertropical Convergence Zone (ITCZ) [e.g., *Garzoli and Richardson, 1989; Fonseca et al., 2004*], which is near the equator during boreal spring and farthest north during boreal summer and fall.

4.2.2. North Equatorial Undercurrent

[27] The NEUC volume transport is highest during boreal spring when its transport reaches 7 Sv (Figure 5b) and lowest in boreal fall (~ 3 – 5 Sv). Although the annual cycle dominates the NEUC transport variability over the semiannual cycle (explained variance: 35% versus 1%; Table 2),

the relatively low-percent variance compared with the NECC suggests that the NEUC is strongly modulated by mesoscale or interannual variability, as there are not enough samples for each month to adequately constrain the seasonal cycle. Compared to the seasonal cycle of NECC volume transport (Figure 5a), the NEUC and the NECC transports bear an almost inverse relationship. In addition, the seasonal cycles of the NEUC volume transport and core velocity seem to be inversely related, with higher values (~ 0.3 m/s) during boreal summer and fall and lower values (~ 0.2 m/s) during boreal spring. The seasonal variability of the NEUC core latitude (Figure 5h) has a dominant semiannual variability (31%), and it reaches its southernmost position ($\sim 4^\circ\text{N}$) during boreal spring at the time of highest transport. Interestingly, it is also in boreal spring when the NECC core is furthest south (Figure 5g) and overlaps with the 3° – 6°N NEUC band, which suggests that some of eastward flow associated with the NECC may be difficult to dissociate from the NEUC flow during this period. This relationship between the NEUC and NECC is consistent with previous modeling and observational studies [e.g., *Elmoussaoui et al.*, 2005; *Brandt et al.*, 2010].

4.2.3. South Equatorial Undercurrent

[28] The XBT-derived SEUC volume transport (Figure 5c) exhibits a smaller amplitude of seasonal cycle in comparison to the NECC and NEUC. Its mean transport is about 7 Sv, which is in good agreement with previous estimates [*Brandt et al.*, 2006; *Fischer et al.*, 2008], and it is weaker (~ 6 Sv) in boreal summer and winter, in agreement with *Reverdin et al.* [1991], and strongest in boreal spring and fall, reaching up to 10 Sv. Therefore, there are indications that the semiannual variability (explained variance: 39%) dominates the SEUC transport variability in the XBT data. The SEUC core velocity is smallest during boreal summer (~ 0.25 m/s), with indications of strengthening (>0.3 m/s) during late boreal spring and fall (Figure 5f). *Fischer et al.* [2008] reported a weaker mean SEUC velocity of about 0.13–0.18 m/s in the central tropical Atlantic but departures from this mean of up to 0.50 m/s have been observed in its core. The mean position of the SEUC core is approximately 4.5°S and although small, its position variability (Figure 5i) follows its transport variability, in that higher transports are associated with a more northern position and vice versa.

4.3. Synthetic Method Validation on Seasonal to Interannual Time Scales

[29] Having discussed the seasonal cycle of the off-equatorial currents using solely the AX08 data, we now compare the three derived variables (volume transport, core velocity, and core latitude) for each current band with the monthly means computed over the 1993–2010 altimetric period obtained from the synthetic method (green curve in Figure 5).

[30] The synthetic estimates for the NECC follow closely the estimates from hydrography for all three variables (Figures 5a, 5d, and 5g). The synthetic NEUC is about 1 Sv weaker and located $\sim 1^\circ$ of latitude further north (Figures 5b and 5h, respectively), but is in phase with the XBT-derived seasonal cycles. On the other hand, the lower NEUC core velocities (~ 0.1 m/s) found during boreal summer/fall in the synthetic estimates (Figure 5e) are not observed in the XBT estimates. The synthetic SEUC

estimates shows reasonable agreement with the XBT seasonal cycle (Figures 5c, 5f, and 5i), but with lower core velocities and apparent stronger annual periodicity than the latter.

[31] Additionally, Figure 5 shows the WOA09 climatology-derived seasonal cycle to provide a means to assess the improvement of the synthetic method over the mean used in the synthetic method calculation (see section 3.2). The synthetic method estimates show a sizeable improvement toward the WOA09 monthly estimates for all currents, as obvious from the WOA09 seasonal cycle for core velocity and transport, which are systematically lower than those from the XBT and the synthetic data. Moreover, the SEUC (Figure 5i) and especially the NEUC (Figure 5h) are not always present in their current bands due to the low horizontal resolution of the climatology. Thus, the correlations provided by the synthetic method, which are here given by the relationships between SLA and the predictands, are able to capture features that are not provided by the mean (climatological) field alone. Therefore, future improvements in the synthetic methodology could be obtained by developing better mean fields or correlations, a well-known problem in statistics [*Gelman et al.*, 2003].

[32] We further validate the synthetic method on seasonal to interannual time scales by comparing the transports of the off-equatorial eastward currents from the 31 XBT transect realizations with their synthetic counterparts (Figure 6). The agreement between the synthetic and XBT transport

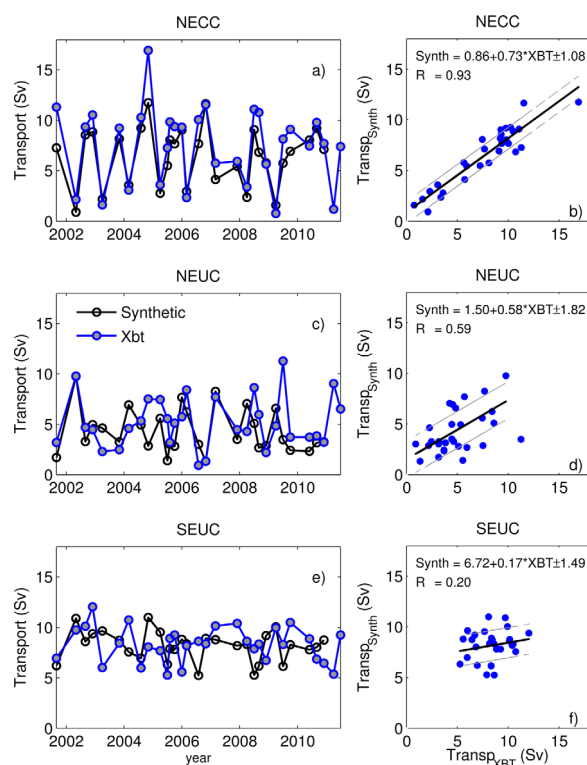


Figure 6. Time series of geostrophic volume transports estimated from the synthetic method (black line with open dots) and from the XBT data (blue dots), with corresponding linear fit between the two transport estimates: (a, b) NECC, (c, d) NEUC, and (e, f) SEUC.

estimates is high for the NECC, with an RMSE = 1.08 Sv (Figures 5a and 5b). A strong linear relationship is found between the two transport estimates and the corresponding linear-correlation coefficient is $R = 0.93$. Regarding the subsurface currents, the synthetic method has considerable skill for the NEUC ($R = 0.59$, RMSE = 1.82 Sv) but the transports using XBT data are generally higher than the synthetic transports (Figures 5c and 5d), as was also observed for their seasonal cycles (Figure 4b). The synthetic method is also able to reproduce a comparable mean SEUC transport of about 7 Sv to the one derived from the XBT data. However, the method fails to reproduce the observed SEUC transport variations (Figures 5e and 5f), with low correlations between the synthetically derived and XBT-derived SEUC transports ($R = 0.20$, RMSE = 1.49 Sv). Due to the low overall agreement, the synthetically derived SEUC estimates are subject to larger uncertainties than the NECC and NEUC estimates on interannual timescales.

4.4. Interannual Variability Using the Synthetically Derived Transports

[33] The tropical Atlantic is subject to a strong seasonal cycle, which influences SST, winds, and SLA in the central

Atlantic region (Figure 7, top). SST varies seasonally, from about 20°C in the southern hemisphere during austral winter and spring, and north of about 7°N during boreal winter and spring, to almost 30°C along the equator in the boreal summer (Figure 7a). The location of the ITCZ, which can be approximated by the zero meridional pseudowind stress contour, follows the seasonal evolution of the warm SSTs in the northern hemisphere, and is located close to the equator from December to July and further north ($\sim 10^\circ\text{N}$) from August to November (Figure 7b). SLA increases during boreal summer and fall months (Figure 7c), which is also associated to mixed layer deepening and its seasonal variability indicates propagation patterns driven by wave mechanisms in the tropical Atlantic. There are indications of strong interannual variability in the region, as observed from large deviations from the seasonal cycle (Figure 7, bottom). During 1999 and 2009, there was strong cooling in the tropical north Atlantic and associated southward shift of the ITCZ and decreased SLA [Foltz *et al.*, 2012]. Warm years in the tropical north Atlantic and equatorial regions occurred in 1998, 2002, 2005, and 2010 (Figure 7a), with the latter being the warmest year on the record for the SST anomalies in the region [Blunden *et al.*, 2011]. These warm

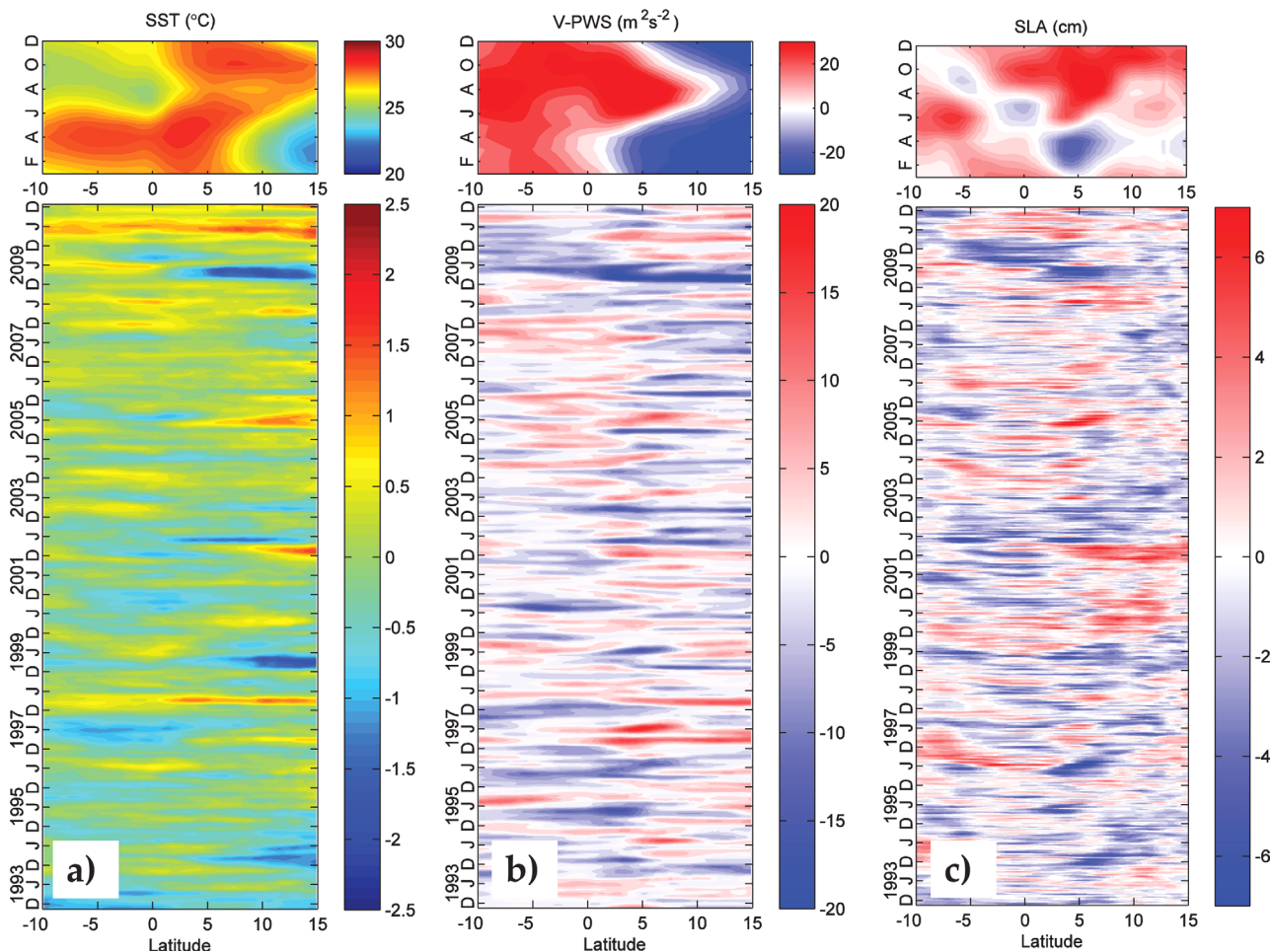


Figure 7. Latitude-time plots of (a) SST [Reynolds *et al.*, 2007], (b) meridional pseudowind stress (V-PWS) [Atlas *et al.*, 2011], and (c) AVISO SLA in the tropical Atlantic. All variables are averaged over 15°W–30°W, which encompasses the region of the AX08 transect. The top portions show the climatological means and the lower portions show anomalies with respect to the climatological means.

events are likewise linked to southerly wind anomalies (Figure 7b) and increased SLA (Figure 7c).

[34] Surface winds influence the circulation through the Rossby and Kelvin wave mechanisms [Foltz and McPhaden, 2010]. The extent to which this variability influences the off-equatorial eastward currents has only been studied for flows near the surface [e.g., Arnault *et al.*, 1999; Fonseca *et al.*, 2004; Hormann *et al.*, 2012]. In the following sections, we use the time series of 7 day synthetically derived transports during 1993–2010 that provide a tool to study the interannual variability of both surface and subsurface off-equatorial eastward currents.

4.4.1. Interannual Signature of the Off-Equatorial Eastward Currents

[35] Characteristics of how the NECC, NEUC, and SEUC vary over time are retrieved by applying a wavelet transform [Torrence and Compo, 1998] to the synthetically derived volume transport time series associated with each current (Figure 8). Wavelet transform analysis of the NECC volume transport time series confirms that the strongest signal is in the annual period band (Figure 8a). Moreover, the energy at the annual period shows intermittent interannual modulation, and a prominent semiannual signal is observed during an event in 1999, when one of the largest NECC transport negative anomalies is followed by one of the largest positive anomalies (Figure 8a, top portion). The event in 1999 has previously been related to a strong wind stress curl anomaly in the western tropical Atlantic during that period [Fonseca *et al.*, 2004]. Regarding the NEUC, wavelet analysis indicates some changes between the 1990s and 2000s, with some amount of energy distributed among semiannual, annual, or longer at the beginning of the record, followed by a decrease in the semiannual variability starting in the early 2000s (Figure 8b). There are further indications of interannual energy modulation in the annual period band in the NEUC transport time series, with increased energy centered on 1995, 2001, and 2006. The SEUC transport also shows a strong annual periodicity (Figure 8c), with largest annual peaks in 1997 and 2004, at times when the NEUC shows weakened variability at this timescale. Wavelet analysis of the zonal pseudowind stress in the equatorial region (Figure 8d) shows a noteworthy resemblance with the NEUC transport in terms of interannual modulation (Figure 8b) in the annual period band.

4.4.2. Relationship Between Synthetic NECC and NEUC Transports and Tropical Atlantic Variability

[36] Here we investigate the correlation between the interannual anomalies of the synthetically derived NECC and NEUC with SST and surface wind stress anomalies in the tropical Atlantic region. We restrict our analysis to the NECC and NEUC transports because they are in better agreement with the XBT estimates on interannual timescales (section 4.3). We use here 7 day transport anomalies relative to the monthly climatology, and gridded 7 day SST and pseudowind stress anomalies from the 1993 to 2010 altimetric period. In this analysis, all data are standardized by subtracting their mean and dividing by their standard deviation as well as low-pass filtered with a 13 point (about 90 days) window moving average to reduce mesoscale variability. Only statistically significant correlation values are taken into account ($P < 0.05$), which corresponds to a 95% significance level using a t -test statistical analysis.

4.4.2.1. North Equatorial Countercurrent

[37] The correlation between the NECC transport and SST anomalies (SSTA) for the 1993–2010 altimetric period produces a distinct pattern in the form of an anomalous meridional SST gradient (Figure 9a), with positive correlation just north of the equator in the ITCZ region, centered at approximately 2°N , 30°W , and extending northeastward, and negative correlation in the central south of the domain, centered at about 20°S , 17°W . The corresponding correlation with pseudowind stress anomalies indicates an anomalous strengthening of the southeasterly trades, with largest magnitude in the western equatorial region. This pattern is reminiscent of the Atlantic meridional mode [e.g., Chang *et al.*, 2006, and references therein], which is believed to be driven by the wind-evaporation-SST feedback mechanism involving interactions between SST changes and wind-induced latent heat fluxes [Xie and Philander, 1994; Chang *et al.*, 1997]. A similar pattern has also been found for the NECC in a recent study using complex empirical-orthogonal function analysis of a near-surface drifter-altimetry synthesis product [Hormann *et al.*, 2012].

[38] An SSTA gradient index (SST1) can be defined by subtracting area averages over the northern (35°W – 15°W / 0° – 5°N) and southern (25°W – 10°W / 12°S – 22°S) boxes marked in Figure 9a. The correlation between the 7 day NECC transport anomalies and SST1 is significant ($R = 0.43$), with maximum negative correlation at zero lag (Figure 9c). A meridional wind-stress index (v -wind1), computed over the northern box described above, which focuses on the variability near the central equatorial region, shows a maximum positive correlation of $R = 0.40$, with the NECC lagging the wind strengthening by two weeks. This relationship suggests that there is a fast response of the NECC and SST to wind anomalies in the index regions that might be explained by either the fast adjustment time of the ocean through equatorial waves [e.g., Ma, 1996] or by anomalies simply advected from the surface NBC retro-reflection region [e.g., Frantantoni *et al.*, 2000; Foltz *et al.*, 2012].

4.4.2.2. North Equatorial Undercurrent

[39] The pattern arising from the correlation between the NEUC transport and both SST and wind stress anomalies (Figure 10a) can be described as follows: negative SST correlation coefficients prevail in the northern part of the basin, with stronger signal in the northeast, while positive correlations are found along the central and eastern equatorial region and in the southeastern part of the basin. In addition, the trades are weakened in the western to central equatorial Atlantic and northeasterly wind anomalies prevail over the Gulf of Guinea for positive NEUC transport anomalies. The obtained meridional gradient SST pattern suggests a relation to the Atlantic meridional mode, and the equatorial SST pattern also indicates a relation to the zonal mode [e.g., Chang *et al.*, 2006, and references therein], further supporting the previously proposed link between these two modes [Servain *et al.*, 1999; Foltz and McPhaden, 2010]. The derived wind stress response interacts with the SST in such a way that the anomalous SSTs shift the ITCZ southward [Moura and Shukla, 1981], reinforcing the positive SST anomaly along the equator [Foltz and McPhaden, 2010]. Consistent with this proposed link, the zonal wind

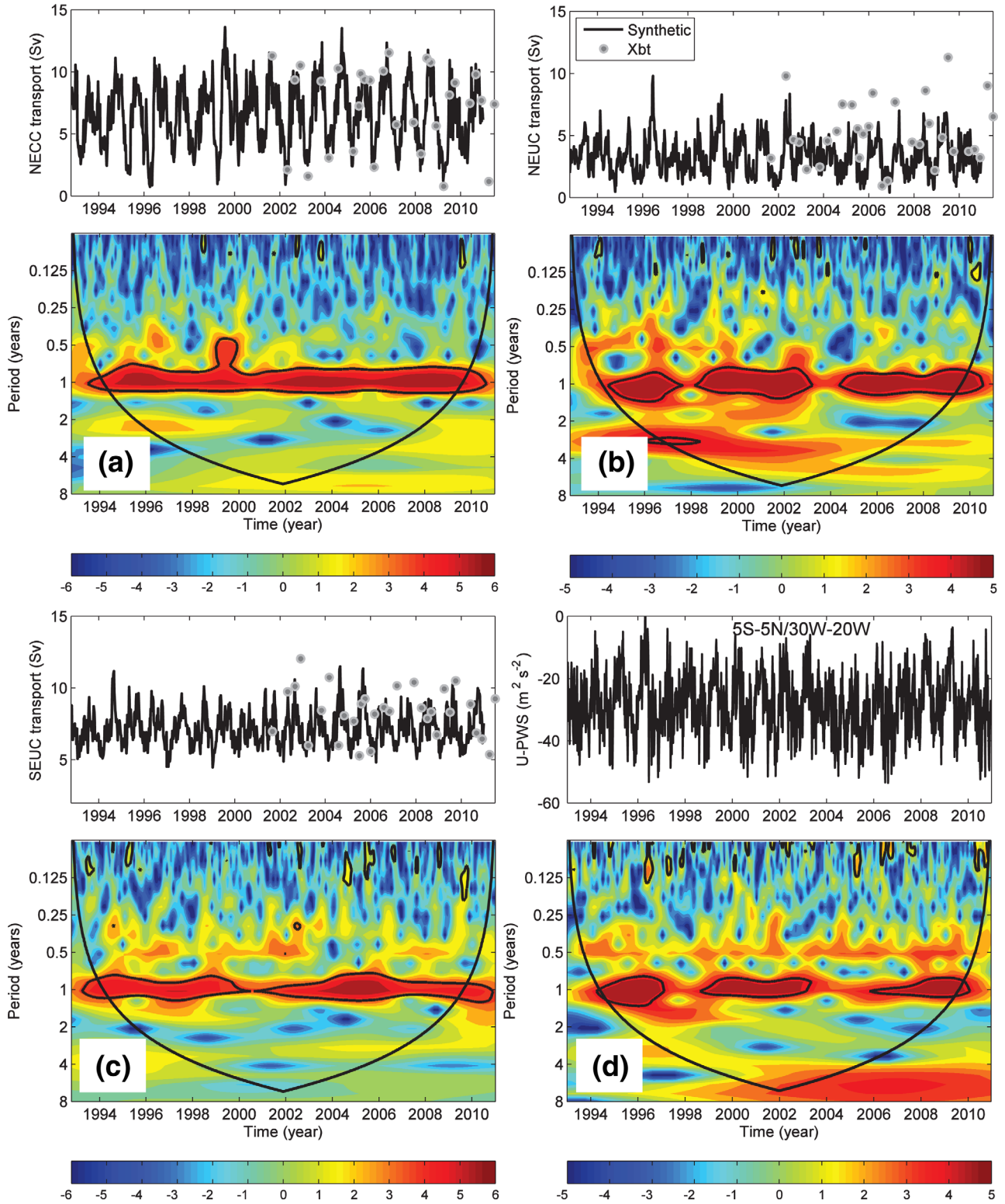


Figure 8. Time series and respective wavelet transforms of the 7 day (a) NECC transport, (b) NEUC transport, (c) SEUC transport, and (d) zonal pseudowind stress averaged over the region 5°S – 5°N / 30°W – 20°W . Top portions show the transport time series as generated by the synthetic method, with the gray circles overlaid for the XBT-derived transports. The wavelet power spectra are based on a Morlet transform and areas above the 95% significance level are encircled by black contours, with the bowl-shaped black lines indicating the cone of influence.

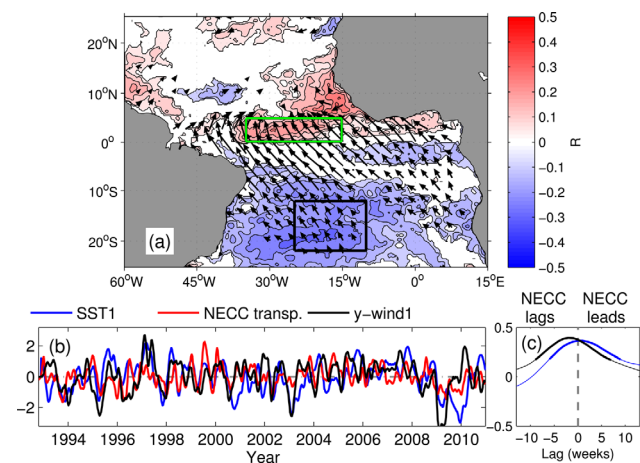


Figure 9. (a) Instantaneous correlation between the standardized NECC transport anomalies and both SSTA (coloring) and pseudowind stress anomalies (vectors). Only statistically significant values are shown. (b) Time series of the standardized NECC transport anomalies (red), SSTA index (SST1, blue), and meridional wind index (y -wind1, black). SST1 is defined by subtracting the averages over the northern (35°W – $15^{\circ}\text{W}/0$ – 5°N) and southern (25°W – $10^{\circ}\text{W}/12^{\circ}\text{S}$ – 22°S) boxes as marked in Figure 9a, and y -wind1 is defined as the average of the meridional pseudowind stress anomalies over the northern box (green box). (c) Lagged correlations of the NECC with the SST1 (blue) and y -wind1 indices (black), with statistically significant values marked by bold lines.

stress in the equatorial region, as defined in our wavelet analysis (Figure 8d), is significantly positively correlated with the NEUC transport ($R=0.43$), leading the NEUC variability by 5 weeks.

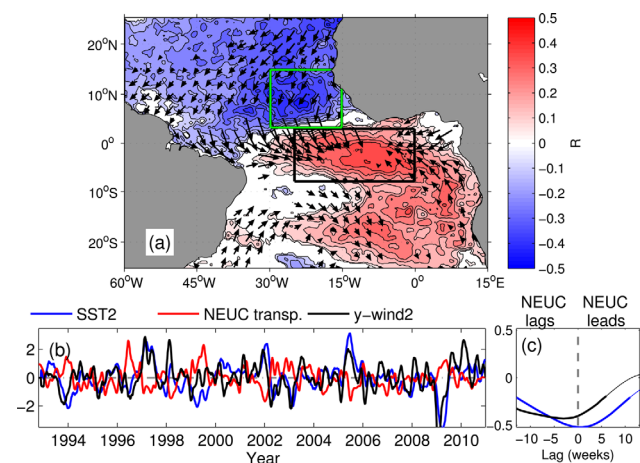


Figure 10. Same as Figure 9, but for NEUC transport anomalies. The SST index (SST2; blue) is defined here as the difference between the northern box average over the Guinea Dome region (5° – $15^{\circ}\text{N}/15^{\circ}$ – 30°W) and the southern box average (8°S – $5^{\circ}\text{N}/30^{\circ}\text{W}$ – 5°E) as marked in Figure 10a, and y -wind2 is defined as the average of the meridional pseudowind stress anomalies over the northern box (green box).

[40] Previous studies that used virtual Lagrangian floats have shown that the NEUC provides waters for the upwelling in the Guinea Dome and equatorial regions [Stramma *et al.*, 2005; Hüttl-Kabus and Böning, 2008]. Results obtained here agree in that negative (positive) NEUC transport anomalies are associated with warm (cold) SSTAs and northeasterly (southwesterly) wind anomalies in the Guinea Dome region (Figure 10a), which are consistent with an decreased (increased) coastal upwelling in this region. As for the NECC, we define a meridional SST gradient index (SST2) and a meridional wind stress index (y -wind2), and relate these indices to the NEUC transport anomalies. We consider here the difference between SSTA in the Guinea Dome region (5° – $15^{\circ}\text{N}/15^{\circ}$ – 30°W) and in the southeastern Atlantic (8°S – $5^{\circ}\text{N}/30^{\circ}\text{W}$ – 5°W) as well as the meridional wind stress average over the Guinea Dome region. We find that the maximum correlation between the NEUC transport anomalies with SST2 and y -wind2 to be $R = -0.51$ (zero lag) and $R = -0.32$ (NEUC lags by 3 weeks), respectively (Figure 10c).

5. Discussion and Conclusions

[41] In the present study, we combined data from the high-density AX08 XBT transect and altimetry to investigate the seasonal and interannual variability of major Atlantic off-equatorial eastward currents, namely the NECC, NEUC, and SEUC.

[42] The seasonal cycles of the off-equatorial eastward currents derived from our analyses of the XBT data alone are in good agreement with previous studies [e.g., Richardson and Reverdin, 1987]. The NECC, defined here between 3°N and 10°N above $\sigma_{\theta} = 24.5 \text{ kg/m}^3$, exhibits a strong annual cycle, with minimum transport and velocity ($\sim 2 \text{ Sv}$ and $\sim 0.2 \text{ m/s}$, respectively) in boreal spring and maximum ($\sim 10 \text{ Sv}$ and $\sim 0.5 \text{ m/s}$) in boreal fall. The synthetic method captures the NECC seasonal cycle with good skill. On interannual timescales, synthetic estimates show that an increased NECC transport is linked to a strengthening of the southeasterly trades (at a 2 week lag) and a positive meridional SST gradient pattern (i.e., warmer tropical North Atlantic and colder tropical South Atlantic) at zero lag, consistent with Hormann *et al.* [2012]. The NECC strengthening associated with such a meridional SST gradient might act as a positive feedback, since it would increase the eastward transport of warmer western waters toward the region of maximum SST gradient.

[43] The NEUC seasonal cycle from the XBT data is characterized by stronger transports during boreal spring/summer (up to 7 Sv), which is in opposite phase to the NECC transport cycle. The NEUC core is mostly located between 4° and 6°N , with maximum velocities of about 0.30 m/s in June–July. Synthetic estimates of the transport and position seasonal cycles follow the phase of the XBT estimates but are slightly weaker and more northward ($\sim 1 \text{ Sv}$ and $\sim 1^{\circ}$ of latitude, respectively). The synthetic core velocity is reduced during boreal fall ($\sim 0.12 \text{ m/s}$), which may be an improvement over the XBT-only estimates, since it follows closer the phase of transport variability and is less subject to mesoscale aliasing. Synthetic estimates of the NEUC transport suggest that there is a decrease in the

semiannual variability since 2000, which follows years of mixed semiannual, annual, and longer period variability, and that throughout the record there has been an interannual modulation of the annual variability. The latter is also in agreement with anomalous zonal wind stress variability in the western-central equatorial Atlantic (Figure 8d). Our results further indicate that the interannual variability of the NEUC transport is statistically related to the difference between positive SST anomalies in the equatorial Atlantic and negative SST anomalies in the Guinea Dome region, similar to the negative index of the Atlantic meridional mode [Foltz *et al.*, 2012]. Such a link between the NEUC and the Guinea Dome has long been proposed [e.g., Voituriez, 1981; Schott *et al.*, 2004], since the uplifting of the thermal structure in the dome extends much further down than the thermocline. The strong upwelling in this region is, for instance, related to the outcropping of the $\sigma_\theta = 24.5$ kg/m³ isopycnal [Inui *et al.*, 2002]. The underlying mechanism of this relationship might be that a cooler Guinea Dome and warmer equatorial region increase the north-south density gradient in the NEUC region, and strengthen its core. Some model studies in the Pacific indeed suggest that the coastal upwelling on the eastern side of the basin can drive the variability of such a current [e.g., McCreary *et al.*, 2002].

[44] The NEUC and NECC exhibit an inverse relationship in transport variability on interannual timescales. Both are linked to the variability of the cross-equatorial wind stress, but the NECC is strengthened in association with increased southeasterly winds whereas increases in the NEUC are associated with reduced southeasterly winds. The interannual modes of tropical Atlantic variability are strongly tied to their seasonal cycle [e.g., Nobre and Shukla, 1996; Servain *et al.*, 1999], which is consistent with the fact that this inverse relationship between the NEUC and NECC transports also holds for the seasonal cycle. Our results suggest that the NECC overlaps latitudinally and may interact with the NEUC, especially during boreal winter/spring when the NECC is displaced furthest south.

[45] The SEUC is located on average at about 4.5°S and exhibits a rather weak seasonal cycle, with a mean transport of about 7 Sv. The XBT data show a stronger semiannual cycle of velocity and transport, with higher values during spring and fall (~ 0.3 m/s and 10 Sv, respectively). The synthetic method produces a comparable SEUC climatology, but with decreased semiannual component in transport, and weaker mean velocities (~ 0.25 m/s). Although the synthetic method produces a comparable SEUC climatology, the correlation with the XBT-derived transport is rather small. There are indications of an out-of-phase relationship between the NEUC and SEUC on interannual timescales, but the synthetic method is subject to higher uncertainty in reproducing the SEUC variability. The somewhat limited ability of our methodology to reproduce SEUC variations is a consequence of the weak SLA variability in the southern tropical Atlantic (Figure 1a). As a result, the surface signature of the SEUC is masked by compensating effects in the water column (Figure 2). The compensating effects can be explained by, for example, buoyancy and wind forcing components of the same magnitude and opposing signs [Mayer *et al.*, 2001]. Therefore,

regular hydrographic sampling is particularly important for monitoring the SEUC.

[46] Our results indicate that due to strong regional intra-seasonal variability generated by mesoscale variability (eddies, passage of TIWs, etc.), more XBT sections are needed to produce more robust estimates of the seasonal cycle of these currents using XBT data only. For instance, out of the 31 analyzed XBT sections only one realization is available for January, May, and June, and no section is yet available for February. The synthetic method applied here have potential to improve considerably upon estimates of the seasonal evolution of the off-equatorial eastward currents, and can overcome the sampling restrictions, and potentially produce better estimates of the long-term evolution of these currents.

[47] Results from this study are subject to specific caveats that provide avenues for future research: first, we use a simple statistical method to infer the relationship between surface height and ocean properties at depth. Using an improved statistical method and a more structured mean field (instead of the coarse spatial-resolution WOA09) may allow for including additional information, such as latitudinal cross-correlation between and autocorrelation of the residuals at depth, as well as the use of additional constraints derived from collocated observations. Second, we use empirical estimates of salinity inferred from a climatological T-S relationship at each location, and climatological values of dynamic height at 800 m to obtain absolute dynamic heights from the XBT data. Available observations from the Argo network, for example, could reduce the salinity inference errors associated with this methodology. However, these observations are mostly restricted to the last 5–6 years and do not cover the whole period of XBT observations. Third, eddy-resolving altimetry fields from multiple satellite missions are required to adequately monitor the equatorial current system. Finally, high-resolution modeling can fill gaps in the observational space and examine in a dynamically consistent fashion the implications of our results.

[48] This study highlights the value of using multiplatform observations to assess the importance of ocean dynamics to drive variations in surface properties such as SSTs, which are critical for weather and climate studies.

Appendix A

A1. Estimation of Errors in the XBT Measurements

[49] The methodology applied in this study is subject to several sources of error, which are quantified in this section. The most important of these errors are related to the XBT temperature data precision, depth accuracy of the FRE, salinity inference, and the SLA data precision when applying the synthetic method. Here we use established estimates of these measurement errors, and assess how they can affect dynamic height estimates and the derived velocity. The typical error values, listed in Table A1, were obtained from several scientific papers [e.g., Ducet *et al.*,

Table A1. Summary of Figure A1^a

Variable (Error)	Error Distribution	Surface		300 m	
		σ_{DH} (cm)	σ_V (m/s)	σ_{DH} (cm)	σ_V (m/s)
T ($\sigma_T = 0.1^\circ\text{C}$)	$\Delta T = N(0, \sigma_T^2)$	0.15	0.016	0.09	0.01
S ($\sigma_S = 0.3$ psu)	$\Delta S = N(0, \sigma_S^2)$	0.89	0.095	0.71	0.076
Z ($\sigma_{Z0} = 5$ m; $\sigma_{Z1} = 2\%$ of depth)	$\Delta Z = \text{Unif}([- \sigma_{Z0}, \sigma_{Z0}]) + N(0, \sigma_{Z1}^2)$	1.94	0.078	1.26	0.035
Total	$\Delta T_{\text{Tot}} = E_{\text{TEMP}} + E_{\text{SAL}} + E_Z$	2.19	0.124	1.46	0.084
SLA ($\sigma_{\text{SLA}} = 2$ cm; $\lambda = 300$ km)	$\Delta \text{SLA} = N(0, \Sigma), \Sigma = (\sigma_{\text{SLA}}^2) \exp(-d/\lambda)$	2.09	0.171	–	–

^aThe first column displays the typical measurement errors applied for each variable and the second one specifies the used error distribution, with N and Unif denoting Gaussian and uniform distributions, respectively. The remaining columns are the confidence intervals defined as one standard deviation of the dynamic height (σ_{DH}) and velocity (σ_V) fields at the surface and 300 m depth. The $1-\sigma$ levels have been derived from a bootstrap analysis with 300 samples.

2000; *Goni and Baringer, 2002; Goes et al., 2013*). According to the manufacturer (Sippican/Lockheed Martin), the XBT measurement error for temperature precision is $\sigma_T = 0.1^\circ\text{C}$, and the maximum tolerance for the depth error associated with the FRE is approximately linear with depth, either $\sigma_z = 5$ m or 2% of depth, whichever is greater. The salinity inference error has been shown to be among the largest contributors to the dynamic height error [*Goni and Baringer, 2002*], with typical differences of $\sigma_S = 0.3$ psu between in situ and climatological salinity estimates resulting in dynamic height differences as large as $\sigma_{DH} = 5$ cm. As stated in section 2, the average RMSE for the AVISO SLA product is typically on the order of $\sigma_{\text{SLA}} = 2$ cm [*Cheney et al., 1994; Ducet et al., 2000*]. *Arnault et al. [1999]* estimated that a SLA error of 2 cm would result in velocity errors, ranging from 0.05 m/s to 0.30 m/s between 7.5°N and the equator.

[50] In our assessment, we use one of the AX08 sections with its associated salinity estimated from the climatological T-S relationships (i.e., using the methodology of *Thacker [2007a, 2007b]*); cf. section 2a) as the “true” section. Results obtained here are for the regions between 3° and 10° of latitude, encompassing the locations of the off-equatorial eastward currents, and are not dependent on which AX08 section is chosen. We perturb the “true” section with stochastic noise (Table A1), and apply a bootstrap method with 300 samples. The error distributions are assumed as follows:

[51] (i) Temperature and salinity errors (ΔT and ΔS in Table A1, respectively) are assumed to be derived from an uncorrelated Gaussian noise ($\Delta T \approx \Delta S \approx N(0, \sigma^2)$) with zero mean and standard deviations σ , using as σ the typical XBT measurement error values (σ_T and σ_S , respectively).

[52] (ii) XBT depth errors (ΔZ) are related to biases in the FRE which are highly dependent on the timing and the region of each cruise [*Reverdin et al., 2009*]. This is because the FRE depends on the type and manufacturing year of the XBT probes, which can vary from one cruise to the next, and on the viscosity and stratification of the water in the region. We approximate the XBT depth errors by a linear depth bias ($\Delta Z = \Delta Z_0 + \Delta Z_1 \times Z$), where the linear coefficient (ΔZ_1) is dependent on the probe and regional characteristics, and the intercept or depth offset (ΔZ_0) related to surface phenomena such as wave height variability, entry velocity, and angle of the probe [*Goes et al., 2013*]. Because all the XBTs of an AX08 section are

deployed in a comparable region and are from the same manufacturing year, we assume that ΔZ is generated by the same linear depth bias in each section, varying from section-to-section as an uncorrelated Gaussian noise process ($\Delta Z_1 \approx N(0, \sigma_{Z1}^2)$), plus a depth offset that affects each XBT cast and is drawn from a uniform distribution ($\Delta Z_0 \approx \text{Unif}([- \sigma_{Z0}, \sigma_{Z0}])$). Therefore, the overall depth error is $\Delta Z \approx \Delta Z_0 + \Delta Z_1$.

[53] (iii) SLA measurement errors are assumed to be a spatially correlated Gaussian noise process $\Delta \text{SLA} \approx (N(0, \Sigma))$, following an exponentially decaying covariance matrix $\Sigma = \sigma_{\text{SLA}}^2 \exp(-d/\lambda)$ with a length scale of $\lambda = 300$ km [*Ducet et al., 2000*], and a distance d between two casts.

[54] After perturbing the “true section” with the 300 stochastic samples, the residual distributions of dynamic height (ΔDH) and velocity (Δv) are calculated by subtracting the perturbed sections from the original one (Figure A1), and are here shown for the surface (left) and 300 m depth (right), with the latter approximately corresponding to the depth of the $\sigma_\theta = 26.8$ kg/m³ isopycnal. The altimetric error distribution, ΔSLA , is shown only for the surface level. At the surface, the width of the confidence intervals (CI) given by the standard deviations of ΔDH and Δv (σ_{DH} and σ_v , respectively) indicates that the XBT depth error is the largest contributor to the dynamic height error ($\sigma_{DH} = 1.94$ cm), followed by the salinity error contribution ($\sigma_{DH} = 0.89$ cm) and a small temperature error contribution ($\sigma_{DH} = 0.15$ cm). The total contribution of the XBT dynamic height errors is $\sigma_{DH} = 2.19$ cm, which is slightly higher than the simulated altimetric SLA errors ($\sigma_{DH} = 2.09$ cm). Of great importance here is that the large simulated depth errors do not translate into substantial zonal velocity errors ($\sigma_v = 0.078$ m/s), since horizontal gradients are largely unaffected by the XBT depth biases. The salinity inference is the major cause of velocity errors at the surface ($\sigma_v = 0.095$ m/s), and the total XBT velocity error ($\sigma_v = 0.124$ m/s) is smaller than the altimetric velocity error ($\sigma_v = 0.171$ m/s). At 300 m depth, a similar behavior is found for the dynamic height and velocity errors. However, the magnitude of these errors is reduced since dynamic height is an integral quantity from a reference depth to the surface. The CI of the total XBT errors at that depth is $\sigma_{DH} = 1.46$ cm for dynamic height and $\sigma_v = 0.084$ m/s for velocity, respectively.

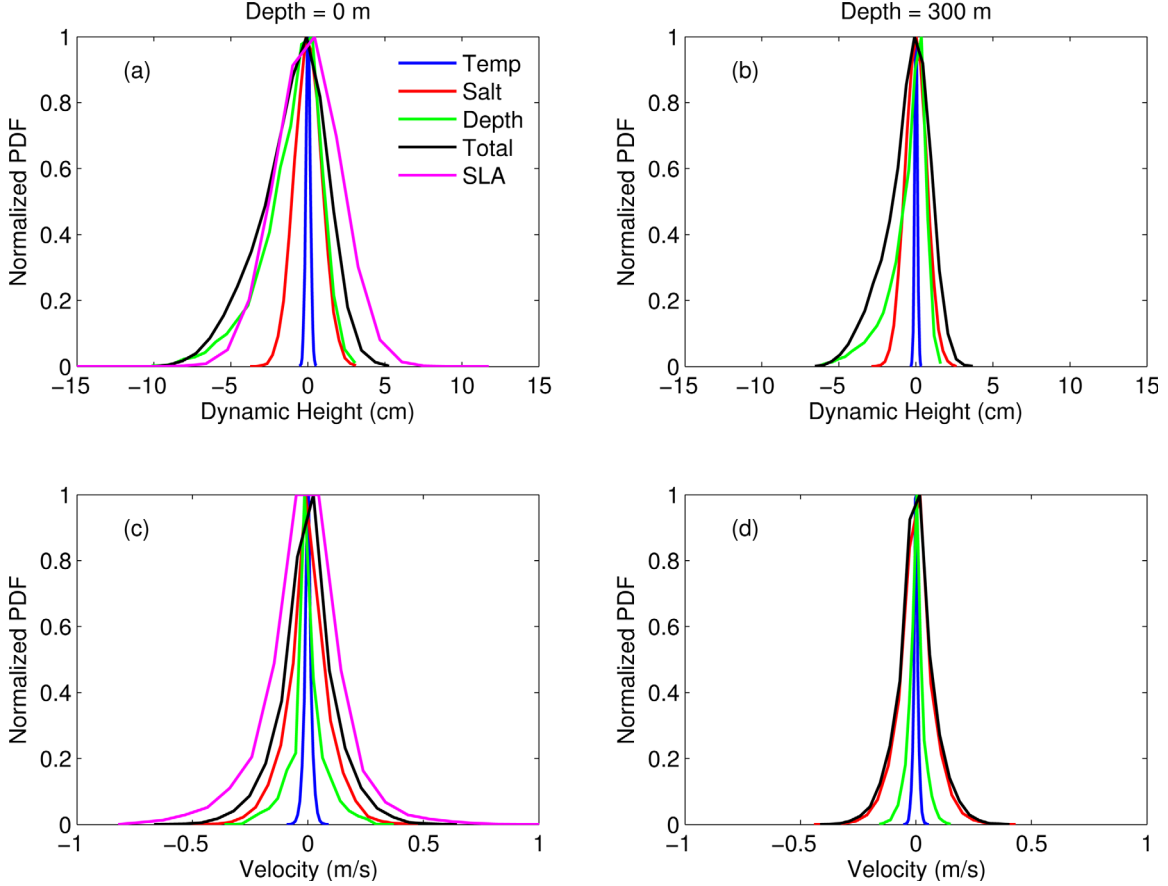


Figure A1. Distribution of the errors in (a, b) dynamic height and (c, d) geostrophic velocity at the surface (Figures A1a and A1c) and 300 m depth (Figures A1b and A1d) that arise from measurement errors associated with XBT (Temp, Salt, Depth, and Total for all three together) and altimetry (SLA) data. SLA error distributions are shown only for the surface.

A2. Velocity Errors Associated With the AX08 Transect Angle

[55] Additional errors result from the assumption that the geostrophic velocity across an oblique transect (Figure 1a) is approximately equal to the zonal geostrophic velocity estimated from a meridional transect. The associated velocity differences have previously been quantified in a similar region to be smaller than 10% of the velocity [Reverdin *et al.*, 1991]. To verify this assumption, we have performed calculations in a $1/12^\circ$ resolution ocean reanalysis (Hycom/NCODA, available at www.hycom.org) [Chassignet *et al.*, 2009], with data spanning from September 2008 to June 2012. Our main goal here is to assess how well the cross-transect velocity represents the true zonal velocity at the location of the AX08 section. In the model output, we simulate the AX08 transect by interpolating the meridional (v) and zonal (u) velocities to the mean AX08 location. Next, we rotate u and v to produce a cross-transect velocity (u'), similar to the one calculated from the AX08 data. The rotation over a transect angle θ is performed as follows:

$$u' = u \cos \theta + v \sin \theta, \quad (\text{A1a})$$

$$v' = -u \sin \theta + v \cos \theta. \quad (\text{A1b})$$

[56] We then compare u' against u by calculating the bias and RMSE between the two velocities (Figures A2a and A2c). The highest biases (0.16–0.2 m/s) and RMSE (0.18–0.2 m/s) between u' and u are observed near the equator extending north to about 4°N . This is because the magnitude and fluctuations of the meridional velocity can be substantial in this region, thus the rotated component shows strong influence from v . Away from the equator, the velocities tend to be fairly comparable, and the bias and RMSE range from 0 to 0.04 m/s and 0.06 to 0.1 m/s, respectively, consistent with weaker meridional velocities. The errors tend to decrease downward since the magnitude of v tends to be stronger closer to the surface.

[57] Moreover, if we rotate u' back to u using only the cosine of the transect angle $u_* = u' \cos(-\theta) = u' \cos(\theta)$ to estimate the true zonal velocity in the absence of v' (Figures A2b and A2d), which cannot be measured using AX08 data, the same error patterns emerge as using only u' , and bias and RMSE actually increase near 4–6 of latitude at certain depths. Thus, the rotation of the cross-transect velocity in the absence of v' measurements does not improve

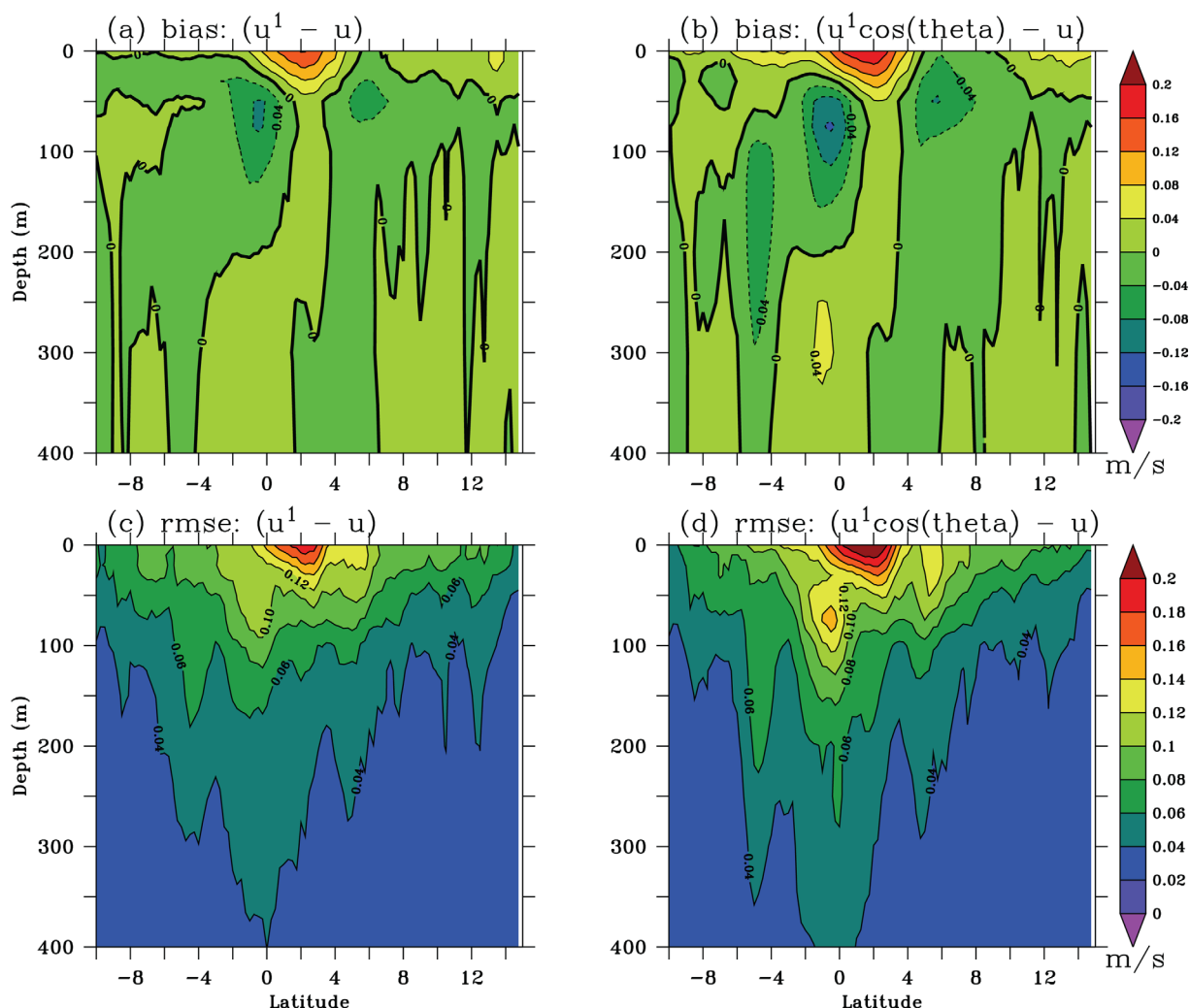


Figure A2. Bias (a, c) and RMSE (c, d) in m/s between the velocity across the AX8 transect (u') and the true zonal velocity (u) at the AX08 location. In Figures A2a and A2c, u' is estimated using a rotation of the zonal (u) and meridional (v) velocity components and in Figures A2b and A2d, u^* is calculated as u' rotated back to the zonal direction neglecting knowledge of the along transect velocity (v'), since this component cannot be estimated from the observed AX08 transect. These results are calculated using the HYCOM/NCODA reanalysis [Chassignet *et al.*, 2009].

the estimation of the true zonal velocity in the region, and is not performed in the present study.

[58] **Acknowledgments.** The authors thank Greg Foltz, Rick Lumpkin, George Halliwell, and Molly Baringer for insightful discussions. This research was carried out under the auspices of the Cooperative Institute for Marine and Atmospheric Studies (CIMAS), a cooperative institute of the University of Miami and the National Oceanic and Atmospheric Administration (NOAA), cooperative agreement NA17RJ1226. This work is supported by NOAA/AOML and NOAA's Climate Program Office. The authors acknowledge the effort of ship crews and logistic personnel.

References

- Arhan, M., A. M. Treguier, B. Boulès, and S. Michel (2006), Diagnosing the annual cycle of the Equatorial Undercurrent in the Atlantic Ocean from a general circulation model, *J. Phys. Oceanogr.*, *36*, 1502–1522.
- Arnault, S., and E. Kestenare (2004), Tropical Atlantic surface current variability from 10 years of TOPEX/Poseidon altimetry, *Geophys. Res. Lett.*, *31*, L03308, doi:10.1029/2003GL019210.
- Arnault, S., B. Boulès, Y. Gouriou, and R. Chuchla (1999), Intercomparison of upper layer circulation of the western equatorial Atlantic Ocean: In situ and satellite data, *J. Geophys. Res.*, *104*, 21,171–21,194.
- Arnault, S., I. Pujol, and J. L. Mélice (2011), In situ validation of Jason-1 and Jason-2 altimetry missions in the tropical Atlantic Ocean, *Mar. Geod.*, *34*, 319–339, doi:10.1080/01490419.2011.584833.
- Athié, G., and F. Marin (2008), Cross-equatorial structure and temporal modulation of intraseasonal variability at the surface of the tropical Atlantic Ocean, *J. Geophys. Res.*, *113*, C08020, doi:10.1029/2007JC004332.
- Athié, G., F. Marin, A.-M. Treguier, B. Boulès, and C. Guivarc'h (2009), Sensitivity of near surface tropical instability waves to sub-monthly wind forcing in the tropical Atlantic, *Ocean Modell.*, *30*, 241–255, doi:10.1016/j.ocemod.2009.06.016.
- Atlas, R., R. N. Hoffman, J. Ardzizzone, S. M. Leidner, J. C. Jusem, D. K. Smith, and D. Gombos (2011), A cross-calibrated, multiplatform ocean surface wind velocity product for meteorological and oceanographic applications, *Bull. Am. Meteorol. Soc.*, *92*, 157–174, doi:10.1175/2010BAMS2946.1.
- Barron, C. N., L. F. Smedstad, J. M. Dastugue, and O. M. Smedstad (2007), Evaluation of ocean models using observed and simulated drifter trajectories: Impact of sea surface height on synthetic profiles for data assimilation, *J. Geophys. Res.*, *112*, C07019, doi:10.1029/2006JC003982.

- Blunden, J., D. S. Arndt, M. O. Baringer (2011), State of the climate in 2010, *Bull. Am. Meteorol. Soc.*, 92, S1–S236, doi:10.1175/1520-0477-92.6.S1.
- Bourlès, B., Y. Gouriou, and R. Chuchla (1999), On the circulation in the upper layer of the western equatorial Atlantic, *J. Geophys. Res.*, 104, 21,151–21,170.
- Bourlès, B., M. D’Orgeville, G. Eldin, Y. Gouriou, R. Chuchla, Y. du Penhoat, and S. Arnault (2002), On the evolution of the thermocline and sub-thermocline eastward currents in the equatorial Atlantic, *Geophys. Res. Lett.*, 29(16), 1785, doi:10.1029/2002GL015098.
- Brandt, P., F. A. Schott, C. Provost, A. Kartavtseff, V. Hormann, B. Bourlès, and J. Fischer (2006), Circulation in the central equatorial Atlantic: Mean and intraseasonal to seasonal variability, *Geophys. Res. Lett.*, 33, L07609, doi:10.1029/2005GL025498.
- Brandt, P., V. Hormann, B. Bourlès, J. Fischer, F. A. Schott, L. Stramma, and M. Dengler (2008), Oxygen tongues and zonal currents in the equatorial Atlantic, *J. Geophys. Res.*, 113, C04012, doi:10.1029/2007JC004435.
- Brandt, P., V. Hormann, A. Körtzinger, M. Visbeck, G. Krahnmann, L. Stramma, R. Lumpkin, and C. Schmid (2010), Changes in the ventilation of the oxygen minimum zone of the tropical North Atlantic, *J. Phys. Oceanogr.*, 40, 1784–1801, doi:10.1175/2010JPO4301.1.
- Brandt, P., A. Funk, V. Hormann, M. Dengler, R. J. Greatbatch, and J. M. Toole (2011), Interannual atmospheric variability forced by the deep equatorial Atlantic Ocean, *Nature*, 473, 497–500, doi:10.1038/nature10013.
- Carnes, M. R., W. J. Teague, and J. L. Mitchell (1994), Inference of subsurface thermocline structure from fields measurable by satellite, *J. Atmos. Oceanic Technol.*, 11, 551–566.
- Carton, J. A., and E. J. Katz (1990), Estimates of the zonal slope and seasonal transport of the Atlantic North Equatorial Countercurrent, *J. Geophys. Res.*, 95, 3091–3100, doi:10.1029/JC095iC03p03091.
- Chang, P., L. Ji, and H. Li (1997), A decadal climate variation in the tropical Atlantic Ocean from thermodynamic air-sea interactions, *Nature*, 385, 516–518.
- Chang, P., et al. (2006), Climate fluctuations of tropical coupled systems—The role of ocean dynamics, *J. Clim.*, 19, 5122–5174, doi:10.1175/JCLI3903.1.
- Chassignet, E. P., et al. (2009), U.S. GODAE: Global Ocean Prediction with the HYbrid Coordinate Ocean Model (HYCOM), *Oceanography*, 22(2), 64–75.
- Cheney, R., L. Miller, R. Agreen, N. Doyle, and J. Lillibridge (1994), TOPEX/Poseidon: The 2-cm solution, *J. Geophys. Res.*, 99, 24,555–24,563.
- Cochrane, J. D., F. J. Kelly Jr., and C. R. Olling (1979), Subthermocline countercurrents in the western equatorial Atlantic Ocean, *J. Phys. Oceanogr.*, 9, 724–738.
- Didden, N., and F. Schott (1992), Seasonal variations in the western tropical Atlantic: Surface circulation from Geosat altimetry and WOCE model results, *J. Geophys. Res.*, 97, 3529–3541.
- Doi, T., T. Tozuka, H. Sasaki, Y. Masumoto, and T. Yamagata (2007), Seasonal and interannual variations of oceanic conditions in the Angola Dome, *J. Phys. Oceanogr.*, 37(11), 2698–2713.
- Ducet, N., P.-Y. Le Traon, and G. Reverdin (2000), Global high resolution mapping of ocean circulation from Topex/Poseidon and ERS-1 and –2, *J. Geophys. Res.*, 105, 19,477–19,498.
- Düing, W., P. Hisard, E. Katz, J. Meincke, L. Miller, K. V. Moroshkin, G. Philander, A. A. Ribnikov, K. Voigt, and R. Weisberg (1975), Meanders and long waves in the equatorial Atlantic, *Nature*, 257, 280–284, doi:10.1038/257280a0.
- Elmoussaoui, A., M. Arhan, and A.-M. Tréguier, (2005), Model-inferred upper ocean circulation in the eastern tropics of the North Atlantic, *Deep Sea Res. I*, 52(7), 1093–1120, doi:10.1016/j.dsr.2005.01.010.
- Fischer, J., V. Hormann, P. Brandt, F. A. Schott, B. Rabe, and A. Funk (2008), South Equatorial Undercurrent in the western to central tropical Atlantic, *Geophys. Res. Lett.*, 35, L21601, doi:10.1029/2008GL035753.
- Foltz, G. R., S. A. Grodsky, and J. A. Carton (2003), Seasonal mixed layer heat budget of the tropical Atlantic Ocean, *J. Geophys. Res.*, 108(C5), 3146, doi:10.1029/2002JC001584.
- Foltz, G., J. Carton, and E. P. Chassignet (2004), Tropical instability vortices in the Atlantic Ocean, *J. Geophys. Res.*, 109, C03029, doi:10.1029/2003JC001942.
- Foltz, G. R., and M. J. McPhaden (2010), Interaction between the Atlantic meridional and Niño modes, *Geophys. Res. Lett.*, 37, L18604, doi:10.1029/2010GL044001.
- Foltz, G. R., M. J. McPhaden, and R. Lumpkin (2012), A strong Atlantic meridional mode event in 2009: The role of mixed layer dynamics, *J. Clim.*, 25, 363–380, doi:10.1175/JCLI-D-11-00150.1.
- Fonseca, C., G. Goni, W. E. Johns, and E. J. D. Campos (2004), Investigations of the North Brazil Current retroflexion and North Equatorial Countercurrent variability, *Geophys. Res. Lett.*, 31, L21304, doi:10.1029/2004GL020054.
- Fox, D. N., W. J. Teague, C. N. Barron, M. R. Carnes, and C. M. Lee (2002), The Modular Ocean Data Assimilation System (MODAS), *J. Atmos. Oceanic Technol.*, 19, 240–252.
- Frantantoni, D., W. E. Johns, T. L. Townsend, and H. E. Hurlburt (2000), Low latitude circulation and mass transport pathways in a model of the tropical Atlantic Ocean, *J. Phys. Oceanogr.*, 30, 1944–1966.
- Garzoli, S. L., and E. J. Katz (1983), The forced annual reversal of the Atlantic North Equatorial Countercurrent, *J. Phys. Oceanogr.*, 13, 2082–2090.
- Garzoli, S. L., and P. L. Richardson (1989), Low-frequency meandering of the Atlantic North Equatorial Countercurrent, *J. Geophys. Res.*, 94, 2079–2090.
- Gelman, A., J. B. Carlin, H. S. Stern, and D. B. Rubin (2003), *Bayesian Data Analysis*, 2nd ed., CRC Press, London.
- Gilson, J., D. Roemmich, B. Cornuelle, and L.-L. Fu (1998), Relationship of TOPEX/Poseidon altimetric height to steric height and circulation in the North Pacific, *J. Geophys. Res.*, 103, 27,947–27,965, doi:10.1029/98JC01680.
- Goes, M., and I. Wainer (2003), Equatorial currents transport changes for extreme warm and cold events in the Atlantic Ocean, *Geophys. Res. Lett.*, 30(5), 8006, doi:10.1029/2002GL015707.
- Goes, M., R. Molinari, I. C. A. Silveira, and I. Wainer (2005), Retroflexions of the North Brazil Current during February 2002, *Deep Sea Res. I*, 52, 647–667, doi:10.1016/j.dsr.2004.10.010.
- Goes, M., G. Goni, and K. Keller (2013), Reducing biases in XBT measurements by including discrete information from pressure switches, *J. Atmos. Oceanic Technol.*, 30, 810–824, doi:10.1175/JTECH-D-12-00126.1.
- Goni, G., and M. Baringer, (2002), Surface currents in the tropical Atlantic across the high density XBT line AX08, *Geophys. Res. Lett.*, 29(24), 2218, doi:10.1029/2002GL015873.
- Goni, G., and W. E. Johns (2001), A census of North Brazil Current rings observed from TOPEX/POSEIDON altimetry: 1992–1998, *Geophys. Res. Lett.*, 28(1), 1–4.
- Goni, G., S. Kamholtz, S. Garzoli, and D. Olson (1996), Dynamics of the Brazil-Malvinas confluence based on inverted echo sounders and altimetry, *J. Geophys. Res.*, 101, 16,273–16,289.
- Gourcuff, C., P. Lherminier, H. Mercier, and P.-Y. Le Traon (2011), Altimetry combined with hydrography for ocean transport estimation, *J. Atmos. Oceanic Technol.*, 28(10), 1324–1337.
- Grodsky, S. A., J. A. Carton, C. Provost, J. Servain, J. A. Lorenzetti, and M. J. McPhaden (2005), Tropical instability waves at 0°N, 23°W in the Atlantic: A case study using Pilot Research Moored Array in the Tropical Atlantic (PIRATA) mooring data, *J. Geophys. Res.*, 110, C08010, doi:10.1029/2005JC002941.
- Guinehut, S., P.-Y. Le Traon, and G. Larnicol (2006), What can we learn from global altimetry/hydrography comparisons?, *Geophys. Res. Lett.*, 33, L10604, doi:10.1029/2005GL025551.
- Hanawa, K., P. Raul, R. Bailey, A. Sy, and M. Szabados (1994), Calculation of new depth equations for expendable bathythermographs using a temperature-error-free method (Application to Sippican/TSK T-7, T-6 and T-4 XBTs), Tech. Pap. Mar. Sci. 67, 46 pp., UNESCO, Paris.
- Hazeleger, W., P. de Vries, and Y. Friocourt (2003), Sources of the Equatorial Undercurrent in the Atlantic in a high-resolution ocean model, *J. Phys. Oceanogr.*, 33, 677–693.
- Hisard, P., and C. Hénin (1987), Response of the equatorial Atlantic Ocean to the 1983–1984 wind from the Programme Français Océan et Climat Dans l’Atlantique Equatorial cruise data set, *J. Geophys. Res.*, 92, 3759–3768.
- Hormann, V., and P. Brandt (2007), Atlantic Equatorial Undercurrent and associated cold tongue variability, *J. Geophys. Res.*, 112, C06017, doi:10.1029/2006JC003931.
- Hormann, V., R. Lumpkin, and G. R. Foltz (2012), Interannual North Equatorial Countercurrent variability and its relation to tropical Atlantic climate modes, *J. Geophys. Res.*, 117, C04035, doi:10.1029/2011JC007697.
- Hsin, Y.-C., and B. Qiu (2012), Seasonal fluctuations of the surface North Equatorial Countercurrent (NECC) across the Pacific basin, *J. Geophys. Res.*, 117, C06001, doi:10.1029/2011JC007794.

- Hua, B. L., F. Marin, and R. Schopp (2003), Three-dimensional dynamics of the subsurface countercurrents and equatorial thermostat. Part I: Formulation of the problem and generic properties, *J. Phys. Oceanogr.*, **33**, 2588–2609.
- Hüttl-Kabus, S., and C. W. Böning (2008), Pathways and variability of the off-equatorial undercurrents in the Atlantic Ocean, *J. Geophys. Res.*, **113**, C10018, doi:10.1029/2007JC004700.
- Inui, T., A. Lazar, P. Malanotte-Rizzoli, and A. Busalacchi (2002), Wind stress effects on subsurface pathways from the subtropical to tropical Atlantic, *J. Phys. Oceanogr.*, **32**, 2257–2276.
- Jochum, M., and P. Malanotte-Rizzoli (2004), A new theory for the generation of the equatorial subsurface undercurrents, *J. Phys. Oceanogr.*, **34**, 755–771.
- Johnson, R. W. (2001), An introduction to Bootstrap, *Teach. Stat.*, **23**(2), 49–54.
- Katz, E. J. (1987), Seasonal response of the sea surface to wind in the equatorial Atlantic, *J. Geophys. Res.*, **92**, 1885–1893.
- Kirchner, K., M. Rhein, S. Hüttl-Kabus, and C. W. Böning (2009), On the spreading of South Atlantic Water into the Northern Hemisphere, *J. Geophys. Res.*, **114**, C05019, doi:10.1029/2008JC005165.
- Kolodziejczyk, N., B. Bourlès, F. Marin, J. Grelet, and R. Chuchla (2009), Seasonal variability of the Equatorial Undercurrent at 10°W as inferred from recent in situ observations, *J. Geophys. Res.*, **114**, C06014, doi:10.1029/2008JC004976.
- Lagerloef, G., G. T. Mitchum, R. B. Lukas, and P. Niiler (1999), Tropical Pacific near surface currents estimated from altimeter, wind and drifter data, *J. Geophys. Res.*, **104**, 23,313–23,326.
- Le Traon P.-Y., F. Nadal, and N. Ducet (1998), An improved mapping method of multisatellite altimeter data, *J. Atmos. Oceanic Technol.*, **15**, 522–533, doi:10.1029/2005GL025551.
- Leuliette, E., and L. Miller (2009), Closing the sea level rise budget with altimetry, Argo, and GRACE, *Geophys. Res. Lett.*, **36**, L04608, doi:10.1029/2008GL036010.
- Locarnini, R. A., A. V. Mishonov, J. I. Antonov, T. P. Boyer, H. E. Garcia, O. K. Baranova, M. M. Zweng, and D. R. Johnson (2010), *World Ocean Atlas 2009, vol. 1, Temperature, NOAA Atlas NESDIS, vol. 68*, edited by S. Levitus, 184 pp., NOAA, Silver Spring, Md.
- Lumpkin, R., and S. L. Garzoli (2005), Near-surface circulation in the tropical Atlantic Ocean, *Deep Sea Res. I*, **52**(3), 495–518.
- Ma, H. (1996), The dynamics of North Brazil Current retroreflection eddies, *J. Mar. Res.*, **54**, 35–53.
- Marin, F., F. Schopp, and B. L. Hua (2003), Three-dimensional dynamics of the subsurface countercurrents and equatorial thermostat. Part II: Influence of the large-scale ventilation and equatorial winds, *J. Phys. Oceanogr.*, **33**, 2610–2626.
- Mayer, D., R. L. Molinari, and M. O. Baringer (2001), Transition regions and their role in the relationship between sea surface height and subsurface temperature structure in the Atlantic Ocean, *Geophys. Res. Lett.*, **28**(20), 3943–3946.
- McCarthy, M. C., L. D. Talley, and D. Roemmich (2000), Seasonal to interannual variability from expendable bathythermograph and TOPEX/Poseidon altimeter data in the South Pacific subtropical gyre, *J. Geophys. Res.*, **105**, 19,535–19,550, doi:10.1029/2000JC900056.
- McCreary, J. P., P. Lu, and Z. Yu (2002), Dynamics of the Pacific subsurface countercurrents, *J. Phys. Oceanogr.*, **32**, 2379–2404.
- Menkes, C. E., et al. (2002), A whirling ecosystem in the equatorial Atlantic, *Geophys. Res. Lett.*, **29**(11), 1553, doi:10.1029/2001GL014576.
- Metcalfe, W., and M. C. Stalcup (1967), Origin of the Atlantic Equatorial Undercurrent, *J. Geophys. Res.*, **72**(20), 4959–4975.
- Molinari, R. L. (1982), Observations of eastward currents in the tropical South Atlantic Ocean: 1978–1980, *J. Geophys. Res.*, **87**, 9707–9714.
- Molinari, R. L. (1983), Observation of near surface currents and temperature in the central and western tropical Atlantic Ocean, *J. Geophys. Res.*, **88**, 4433–4438.
- Moura, A. D., and J. Shukla (1981), On the dynamics of droughts in Northeast Brazil—Observations, theory and numerical experiments with a general-circulation model, *J. Atmos. Sci.*, **38**, 2653–2675.
- Nobre, P., and J. Shukla (1996), Variations of sea surface temperature, wind stress and rainfall over the tropical Atlantic and South America, *J. Clim.*, **9**, 2464–2479.
- Peterson, R. G., and L. Stramma (1991), Upper-level circulation in the South Atlantic Ocean, *Prog. Oceanogr.*, **26**, 1–73.
- Philander, S. G. H., and R. C. Pacanowski (1986), A model of the seasonal cycle in the tropical Atlantic Ocean, *J. Geophys. Res.*, **91**, 14,192–14,206.
- Phillips, H. E., and S. R. Rintoul (2002), A mean synoptic view of the subantarctic front south of Australia, *J. Phys. Oceanogr.*, **32**(5), 1536–1553.
- Pond, S., and G. Pickard (1983), *Introductory Dynamical Oceanography*, 2nd ed., Pergamon, New York.
- Reverdin, G., P. Rual, Y. du Penhoat, and Y. Gouriou (1991), Vertical structure of the seasonal cycle in the central equatorial Atlantic Ocean: XBT sections from 1980 to 1988, *J. Phys. Oceanogr.*, **21**, 277–291.
- Reverdin, G., F. Marin, B. Bourlès and P. L’Herminier (2009), XBT temperature errors during French research cruises (1999–2007), *J. Atmos. Oceanic Technol.*, **26**, 2462–2473, doi:10.1175/2009JTECHO655.1.
- Reynolds, R. W., T. M. Smith, C. Liu, D. B. Chelton, K. S. Casey, and M. G. Schlax (2007), Daily high-resolution-blended analyses for sea surface temperature, *J. Clim.*, **20**, 5473–5496.
- Richardson, P. L., and D. Walsh (1986), Mapping climatological seasonal variations of surface currents in the tropical Atlantic using ship drifts, *J. Geophys. Res.*, **91**, 10,537–10,550.
- Richardson, P., and G. Reverdin (1987), Seasonal cycle of velocity in the Atlantic North Equatorial Countercurrent as measured by surface drifters, current meters and ship drifts, *J. Geophys. Res.*, **92**, 3691–3708.
- Richardson, P. L., S. Arnault, S. Garzoli, and J. G. Bruce (1992), Annual cycle of the Atlantic North Equatorial Countercurrent, *Deep Sea Res.*, **39**(6), 997–1014.
- Ridgway, K. R., and J. R. Dunn (2010), Using satellite altimetry to correct mean temperature and salinity fields derived from Argo floats in the ocean regions around Australia, *Deep Sea Res. I*, **57**, 1137–1151, doi:10.1016/j.dsr.2010.05.010.
- Ridgway, K. R., R. C. Coleman, R. J. Bailey, and P. Sutton (2008), Decadal variability of East Australian Current transport inferred from repeated high-density XBT transects, a CTD survey and satellite altimetry, *J. Geophys. Res.*, **113**, C08039, doi:10.1029/2007JC004664.
- Rintoul, S. R., S. Sokolov, and J. Church (2002), A 6 year record of baroclinic transport variability of the Antarctic Circumpolar Current at 140°E derived from expendable bathythermograph and altimeter measurements, *J. Geophys. Res.*, **107**(C10), 3155, doi:10.1029/2001JC000787.
- Rio, M. H., S. Guinehut, and G. Larnicol (2011), New CNES-CLS09 global mean dynamic topography computed from the combination of GRACE data, altimetry, and in situ measurements, *J. Geophys. Res.*, **116**, C07018, doi:10.1029/2010JC006505.
- Schott, F., L. Stramma, and J. Fischer (1995), The warm water inflow into the western tropical Atlantic boundary regime, spring 1994, *J. Geophys. Res.*, **100**, 24,745–24,760.
- Schott, F., J. Fischer, and L. Stramma (1998), Transports and pathways of the upper-layer circulation in the western tropical Atlantic, *J. Phys. Oceanogr.*, **28**, 1904–1928.
- Schott, F. A., M. Dengler, P. Brandt, K. Affler, J. Fischer, B. Bourlès, Y. Gouriou, R. L. Molinari, and M. Rhein (2003), The zonal currents and transports at 35°W in the tropical Atlantic, *Geophys. Res. Lett.*, **30**(7), 1349, doi:10.1029/2002GL016849.
- Schott, F., J. McCreary, and G. Johnson (2004), Shallow overturning circulations of the tropical-subtropical oceans, in *Earth Climate: The Ocean-Atmosphere Interaction*, edited by C. Wang, S.-P. Xie, and J. A. Carton, AGU Geophys. Monogr. Ser., **147**, 261–304.
- Servain, J., I. Wainer, J. P. McCreary, and A. Dessier (1999), A relationship between the equatorial and meridional modes of climatic variability in the tropical Atlantic, *Geophys. Res. Lett.*, **26**, 485–488, doi:10.1029/1999GL900014.
- Shriver, J. F., and H. E. Hurlburt (2000), The effect of upper ocean eddies on the non-steric contribution to the barotropic mode, *Geophys. Res. Lett.*, **27**, 2713–2716.
- Stramma, L., and M. England (1999), On the water masses and mean circulation of the South Atlantic, *J. Geophys. Res.*, **104**, 20,863–20,833.
- Stramma, L., S. Hüttl, and J. Schafstall (2005), Water masses and currents in the upper tropical northeast Atlantic off northwest Africa, *J. Geophys. Res.*, **110**, C12006, doi:10.1029/2005JC002939.
- Stramma, L., P. Brandt, J. Schafstall, F. Schott, J. Fischer, and A. Körtzinger (2008), Oxygen minimum zone in the North Atlantic south and east of the Cape Verde Islands, *J. Geophys. Res.*, **113**, doi:10.1029/2007JC004369.
- Sutton, R. T., and D. L. R. Hodson (2005), Atlantic Ocean forcing of North American and European summer climate, *Science*, **309**(5731), 115–118, doi:10.1126/JCLI4038.1.
- Thacker, W. C. (2007a), Estimating salinity to complement observed temperature: 1. Gulf of Mexico, *J. Mar. Syst.*, **65**(1–4), 224–248, doi:10.1016/j.jmarsys.2005.06.008.

- Thacker, W. C. (2007b), Estimating salinity to complement observed temperature: 2. Northwestern Atlantic, *J. Mar. Syst.*, 65(1–4), 249–267, doi:10.1016/j.jmarsys.2005.06.007.
- Torrence, C., and G. P. Compo (1998), A practical guide to wavelet analysis, *Bull. Am. Meteorol. Soc.*, 79(1), 61–78.
- Urbano, D. F., M. Jochum, and I. C. A. Silveira (2006), Rediscovering the second core of the Atlantic North Equatorial Countercurrent, *Ocean Modell.*, 12, 1–15, doi:10.1016/j.ocemod.2005.04.003.
- Voituriez, B. (1981), Les sous courants équatoriaux nord et sud et la formation des dômes thermiques tropicaux, *Oceanolog. Acta*, 5, 497–506.
- Weisberg, R., and T. Weingartner (1988), Instability waves in the equatorial Atlantic Ocean, *J. Phys. Oceanogr.*, 18, 1641–1657.
- Willis, J., D. P. Chambers, and R. S. Nerem (2008), Assessing the globally averaged sea level budget on seasonal and interannual timescales, *J. Geophys. Res.*, 113, C06015, doi:10.1029/2007JC004517.
- Xie, S.-P., and S. G. H. Philander (1994), A coupled ocean-atmosphere model of relevance to the ITCZ in the eastern Pacific, *Tellus A*, 46, 340–350.
- Yang, J., and T. M. Joyce (2006), Local and equatorial forcing of seasonal variations of the North Equatorial Countercurrent in the Atlantic ocean, *J. Phys. Oceanogr.*, 36, 238–254.
- Zhang, D., M. J. McPhaden, and W. E. Johns (2003), Observational evidence for flow between the subtropical and tropical Atlantic: The Atlantic subtropical cells, *J. Phys. Oceanogr.*, 33, 1783–1797.